

To be published in the proceedings of the *International School of Subnuclear Physics*
Erice-Sicily, August 29 – September 7, 2001.

The Anomalous Magnetic Moment of the Muon

Vernon W. Hughes (lecturer) and
Ernst P. Sichtermann (scientific secretary)

Department of Physics
Yale University
New Haven, CT 06520-8120

A precise measurement of the anomalous g value, $a = (g - 2)/2$, for the positive muon has been made at the Brookhaven Alternating Gradient Synchrotron. The result $a_{\mu^+} = 11\,659\,202(14)(6) \times 10^{-10}$ (1.3 ppm) is in good agreement with previous measurements and has an error one third that of the combined previous data. The measurement tests standard theory and has the potential to discover new physics. The analysis of data collected in 2000 and 2001 is well underway and, when combined with data from a requested and final run in the fall of 2002 and winter of 2003, are expected to reduce the experimental uncertainty on a_{μ} to 0.4 ppm.

The material in this lecture on the muon $g - 2$ experiment at Brookhaven National Laboratory is presented on behalf of:

The Muon $g - 2$ collaboration: B. Bousquet¹⁰, H.N. Brown², G. Bunce², R.M. Carey¹, P. Cushman¹⁰, G.T. Danby², P.T. Debevec⁸, M. Deile¹², H. Deng¹², W. Deninger⁸, S.K. Dhawan¹², V.P. Druzhinin³, L. Duong¹⁰, E. Efstathiadis¹, F.J.M. Farley¹², G.V. Fedotov³, S. Giron¹⁰, F. Gray⁸, D. Grigoriev³, M. Grosse-Perdekamp¹², A. Grossmann⁷, M.F. Hare¹, D.W. Hertzog⁸, X. Huang¹, V.W. Hughes¹², M. Iwasaki¹¹, K. Jungmann⁶, D. Kawall¹², M. Kawamura¹¹, B.I. Khazin³, J. Kindem¹⁰, F. Krienen¹, I. Kronkvist¹⁰, A. Lam¹, R. Larsen², Y.Y. Lee², I. Logashenko^{1,3}, R. McNabb¹⁰, W. Meng², J. Mi², J.P. Miller¹, W.M. Morse², D. Nikas², C.J.G. Onderwater⁸, Y. Orlov⁴, C.S. Özben², J.M. Paley¹, C. Polly⁸, J. Pretz¹², R. Prigl¹², G. zu Putlitz⁷, T. Qian¹⁰, S.I. Redin¹², O. Rind¹, B.L. Roberts¹, N. Ryskulov³, S. Sedykh⁸, Y.K. Semertzidis², Yu.M. Shatunov³, E.P. Sichtermann¹², E. Solodov³, M. Sossong⁸, A. Steinmetz¹², L.R. Sulak¹, C. Timmermans¹⁰, A. Trofimov¹, D. Urner⁸, P. von Walter⁷, D. Warburton², D. Winn⁵, A. Yamamoto⁹, and D. Zimmerman¹⁰

¹ *Department of Physics, Boston University, Boston, Massachusetts 02215*

² *Brookhaven National Laboratory, Upton, New York, 11973*

³ *Budker Institute of Nuclear Physics, Novosibirsk, Russia*

⁴ *Newman Laboratory, Cornell University, Ithaca, New York 14853*

⁵ *Fairfield University, Fairfield, Connecticut 06430*

⁶ *Kernfysisch Versneller Instituut, Rijksuniversiteit Groningen, NL 9747 AA Groningen, The Netherlands*

⁷ *Physikalisches Institut der Universität Heidelberg, 69120 Heidelberg, Germany*

⁸ *Department of Physics, University of Illinois at Urbana-Champaign, Illinois 61801*

⁹ *KEK, High Energy Accelerator Research Organization, Tsukuba, Ibaraki 305-0801, Japan*

¹⁰ *Department of Physics, University of Minnesota, Minneapolis, Minnesota 55455*

¹¹ *Tokyo Institute of Technology, Tokyo, Japan*

¹² *Department of Physics, Yale University, New Haven, Connecticut 06520*

I. INTRODUCTION

The magnetic moment $\vec{\mu}$ of a particle can be written as

$$\vec{\mu} = \frac{e\hbar}{2mc} g\vec{s}, \quad (1)$$

in which e and m are the particle's charge and mass, \vec{s} is the intrinsic spin angular momentum ($s = 1/2$ for a lepton and for a nucleon) and g is the gyromagnetic ratio. For a Dirac particle $g = 2$. If g does not equal 2, an anomalous g value a is defined:

$$g = 2(1 + a) \quad \text{or} \quad a = \frac{g - 2}{2}. \quad (2)$$

The magnetic moments and g -values of particles have played a central role in the development of modern physics, including quantum electrodynamics, nuclear physics and particle physics. This paper is based on a lecture given for the course on Subnuclear Physics at the Erice School in Sicily, September, 2001.

The electron's spin and magnetic moment were evidenced from the deflection of atoms in an inhomogeneous magnetic field and the observation of fine structure by optical spectroscopy [1, 2]. Within the experimental accuracy the magnetic moment was equal to $e\hbar/(2mc)$ (1 Bohr magneton) and g equaled 2. The proton's spin and magnetic moment were determined from an atomic beam magnetic deflection experiment [3, 4]. The proton spin is $1/2$ and its magnetic moment is $2.8e\hbar/(2Mc)$ in which M is the proton mass. Thus the proton is not a Dirac particle and its anomalous g -value, $a = 1.8$, indicates that the proton is not a point particle but has internal structure.

The discovery from atomic beam magnetic resonance spectroscopy that the electron has a small anomalous g -value, $a_e = 0.00119(5)$ [5], was — together with the Lamb shift [6] and the anomalous value of the hyperfine structure of hydrogen [7] — the stimulus for the development of modern quantum electrodynamics. The process came to be understood as a virtual radiative correction for which in lowest order $a_e = \alpha/(2\pi) = 0.00116$ [8].

The muon also has an anomalous magnetic moment which was first measured in an experiment based on parity nonconservation in the decays $\pi^+ \rightarrow \mu^+ + \nu_\mu$ and $\mu^+ \rightarrow e^+ + \bar{\nu}_\mu + \nu_e$, and it was found that $a_\mu = 0.00119(10)$ [9]. This verified that the muon is a heavy electron with, to within the experimental errors, the same anomalous g -value due to the virtual radiative correction.

Experimental measurements and theoretical calculations of the electron anomalous g -value a_e have achieved very high precision with the uncertainty $\delta a_e \sim 4$ ppb [10]. The experiment is a radiofrequency spectroscopic measurement of the energy levels of a single electron in a magnetic and electric storage bottle (Penning trap), associated with its spin and orbital

motions [11]. The theory is based on a perturbation theory of quantum electrodynamics with expansion parameter α and includes higher order virtual radiative corrections [12]. The agreement of the experimental and theoretical values for a_e provides one of the most sensitive tests of quantum electrodynamics.

Experimental measurements and theoretical calculations of the muon anomalous g -value a_μ have also achieved high precision with the uncertainty $\delta a_\mu \sim 1$ ppm. Several well-known experiments on the muon were done at CERN. The first CERN experiment [9], mentioned above, studied the orbital and spin motion of low momentum (~ 30 MeV/ c) μ^+ in a homogeneous magnetic field, which involved about 2 orbital turns between the entrance and exit of the muons from the field. After this first experiment, which found $a_\mu = 0.001\,19(10)$ and established the leading order radiative contribution, $a_\mu = \alpha/(2\pi)$, a second experiment was done at CERN [13] which utilized a muon storage ring of 1.0 T for muons with $\gamma = 10$ and determined a_μ to 160 ppm. When the theoretical calculation included properly the higher order radiative correction term of order α^2 , including the Feynman diagram for light by light scattering, the experimental and theoretical values agreed. The third and final CERN experiment [14] had a muon magnetic storage ring of 1.47 T, injected pions to produce muons (μ^+ and μ^-) with $\gamma = 30$, and determined a_μ to 7.6 ppm. For the theory it was necessary to calculate the contribution from the modification of the photon propagator due to virtual hadrons. Then the experimental and theoretical values, both with an accuracy of 8 ppm, agreed [10]. Extensive reviews of the CERN experiments are found in Refs. [15, 16]

The goal of the on-going experiment at Brookhaven National Laboratory is to improve the accuracy of the CERN measurement by a factor of 20, to 0.4 ppm. The experiment utilizes a magnetic storage ring of 1.45 T for muons with $\gamma = 30$ with muon injection. A detailed description of this experiment will be given in Section V.

A precise measurement of a_μ of the muon is of great value for comparison with standard theory, because the theory involves all the fundamental interactions — quantum electrodynamics, electroweak interaction, and quantum chromodynamics — in a significant way [10]. Despite the precision of the electron g -value, the muon g -value is more sensitive to standard model extensions, typically by a factor of $(m_\mu/m_e)^2$. The predicted electroweak contribution, not yet observed, should be measured. Many speculative theories beyond the standard model predict deviations of $a_\mu(\text{expt})$ from its theoretical value $a_\mu(\text{SM})$ based on the standard model. A deviation of $a_\mu(\text{expt})$ from $a_\mu(\text{SM})$ indicates new physics, such as lepton structure, W anomalous magnetic moment, supersymmetry, leptoquarks, new particles, or extra dimensions. However, a_μ by itself can not determine the specific cause of such a deviation. Agreement of $a_\mu(\text{expt})$ and $a_\mu(\text{SM})$ places constraints on speculative new theories [10].

Following this section I, the article includes the following sections: Section II, The Electron

Anomalous Magnetic Moment; Section III, Principle of the current muon $g - 2$ experiment; Section IV, Particle Dynamics; Section V, Experimental Set-up at BNL; Section VI, Data Analysis; Section VII, Results; Section VIII, Theoretical Value for a_μ ; Section IX, Comparison of Experiment and Theory; Section X, Contributions Beyond the Standard Model; Section XI, Future; Section XII, Early History of the Experiment at BNL, Our Collaboration; Section XIII, Acknowledgements.

II. THE ELECTRON ANOMALOUS MAGNETIC MOMENT

The current experimental value for a_e comes from an experiment in which a single electron is confined in an electromagnetic trap with a strong magnetic field [11]. The energy levels are determined primarily by the orbital and spin motions of the electron in the strong axial magnetic field $B = 5$ T,

$$W = \mu_0 m_l B + \mu_s m_s B,$$

in which μ_0 and μ_s are the orbital and spin magnetic moments, and m_l and m_s are the components of orbital and spin angular momentum (Fig. 1). Microwave magnetic resonance transitions in which Δm_l and/or $\Delta m_s = \pm 1$ allow the determination of a_e .

A schematic diagram of the apparatus is shown in Fig. 2. Electrons are injected into the trap from a field emission electrode. By repeatedly dumping the trap, a single electron can be isolated with kinetic energy < 1 meV. The resonances are observed through the axial frequency shift. A resonance curve is shown in Fig. 3. The result is

$$a_e(\text{expt}) = 1\,159\,652\,188(4) \cdot 10^{-12} \text{ (4 ppb)}, \quad (3)$$

where the largest uncertainty arises from the potential cavity-mode shift [11]. Further improvement in experimental accuracy will require further understanding and control over the interaction of a single electron with the electromagnetic modes of a surrounding microwave cavity [17].

The theoretical value for a_e is expressed as a power series in α [10, 12, 18]. Feynman diagrams are shown in Fig. 4. Up through 6th order (α^3 term) analytic values are now available for the coefficients [19, 20]. The coefficient of the α^4 term involves the numerical evaluation of 820 Feynman diagrams each with 8 vertices. The result follows:

$$\begin{aligned} a_e(\text{QED} : e, \gamma) = & 0.5 \left(\frac{\alpha}{\pi} \right) - 0.328\,478\,965\,6 \dots \left(\frac{\alpha}{\pi} \right)^2 + \\ & 1.181\,241\,5 \dots \left(\frac{\alpha}{\pi} \right)^3 - 1.509\,8(384) \left(\frac{\alpha}{\pi} \right)^4. \end{aligned} \quad (4)$$

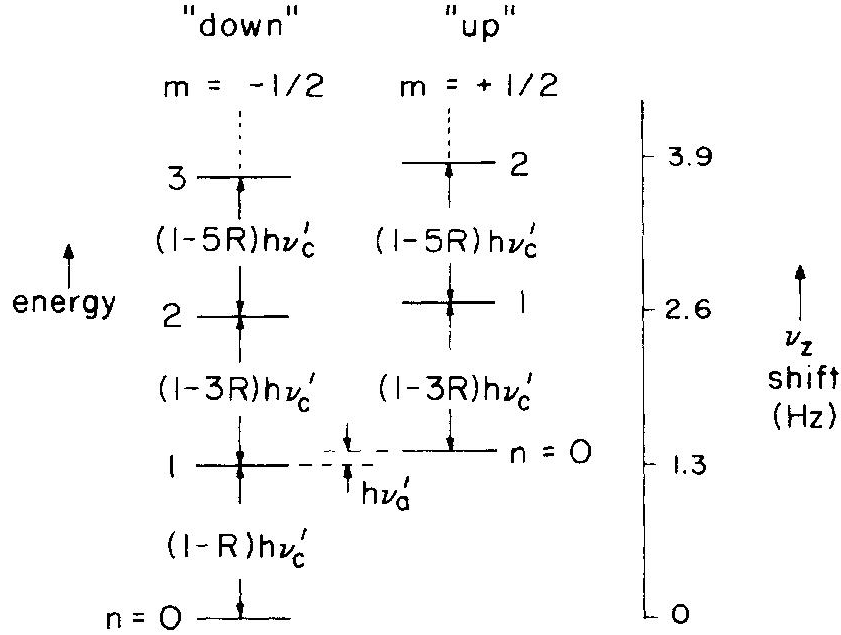


FIG. 1: Lowest Rabi-Landau levels for a geonium atom. The axial frequency (shown in the right-hand scale) corresponds to the coupling via the axial magnetic bottle field. The $h\nu'_c$ energy difference and the relativistic shift ($R = 0.5$ ppb) have been exaggerated for clarity; vanishing axial and magnetron energies are also assumed. The lowest state ($n = 0$) is occupied by the electron or positron 80%–90% of the time. This figure is reproduced from Ref. [11].

The contribution to a_e of all particles heavier than the electron,

$$a_e(\text{QED} : \mu, \tau) + a_e(\text{had}) + a_e(\text{weak}) = 4.393(27) \cdot 10^{-12}, \quad (5)$$

is only at the level of the experimental accuracy 4×10^{-12} . Thus the electron anomalous magnetic moment is a very pure QED problem involving only e^-, e^+ and γ .

To compare $a_e(\text{expt})$ and $a_e(\text{theory})$, a value for α must be determined with high accuracy (~ 4 ppb) by some other experiment. At present methods determine α only to 25 ppb or worse. The values of $a_e(\text{theory})$ using these α values agree with $a_e(\text{expt})$ [18, 21]. Recently, a measurement of the helium fine structure interval 2^3P_1 -to- 2^3P_0 has been reported with a precision of 30 ppb [22], but the theoretical calculation must be improved considerably to determine α to 15 ppb. Perhaps the most promising approach involves a precision measurement of \hbar/M_{Cs} via photon recoil effects in Cesium, which is based on simpler theoretical considerations, [23]. We choose to take QED as valid for a_e , i.e. $a_e(\text{expt}) = a_e(\text{theory})$. Hence, the most accurate value for α is obtained:

$$\alpha^{-1}(a_e) = 137.035\,999\,58(52) \text{ (4 ppb)}. \quad (6)$$

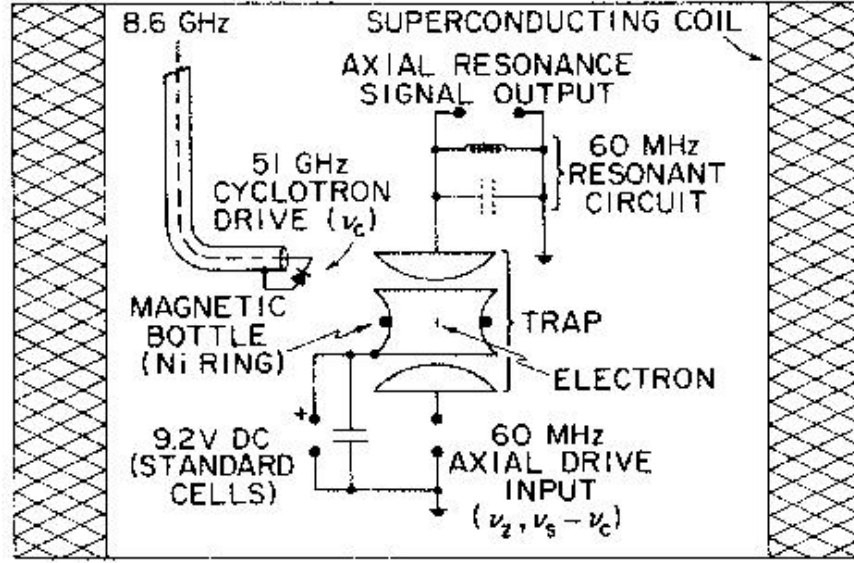


FIG. 2: Schematic of the geonium apparatus. The appropriately biased hyperbolic endcaps and ring electrodes trap the charge axially while coupling the driven harmonic motion to an external LC circuit tuned to the driven axial frequency. Radial trapping of the charge is produced by the strong magnetic field obtained from a superconducting solenoid. This figure is reproduced from Ref. [11].

III. PRINCIPLE OF EXPERIMENT

The principle of the experiment at BNL is the same as that of the last CERN experiment [14] and involves the study of the orbital and spin motions of high energy polarized muons in a magnetic storage ring. Key improvements include the very high intensity of the primary proton beam, the injection of muons instead of pions into the storage ring, and a superferric storage ring magnet.

Longitudinally polarized muons from pion decay are injected into the storage ring which has a homogeneous magnetic field \vec{B} (Fig. 5). In the horizontal plane of the orbit the muon will execute relativistic cyclotron motion with angular frequency ω_c and the muon spin will precess with angular frequency ω_s , which is slightly greater than ω_c by the difference angular frequency $\omega_a = \omega_s - \omega_c$,

$$\omega_c = \frac{eB}{m_\mu c \gamma}, \quad (7)$$

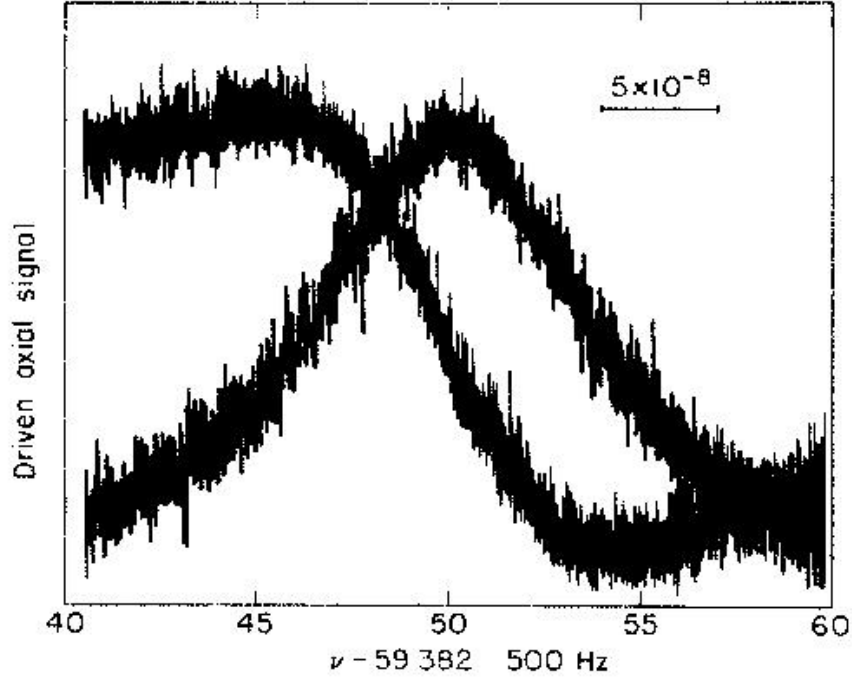


FIG. 3: Axial resonance signals at ≈ 60 MHz. The signal-to-noise ratio of this ≈ 8 Hz wide line corresponds to a frequency resolution of 10 ppb. Both absorption and dispersion modes are shown with the latter mode appropriate for the frequency shift detection scheme employed in these geonium experiments. This figure is reproduced from Ref. [11].

$$\omega_s = \frac{eB}{m_\mu c \gamma} + \frac{e}{m_\mu c} a_\mu B, \quad (8)$$

$$\omega_a = \frac{e}{m_\mu c} a_\mu B, \quad (9)$$

in which $a_\mu = (g_\mu - 2)/2$. The quantity ω_a is designated the muon $g - 2$ frequency. In the experiment ω_a and B are measured; the muon mass m_μ is obtained from an independent experiment on muonium.

In reality vertical focusing must be provided to retain the muons in the storage ring. This is done with an electric quadrupole field \vec{E} in the plane normal to the particle orbit, which modifies ω_a according to

$$\vec{\omega}_a = \frac{e}{mc} \left(a_\mu \vec{B} - \left[a_\mu - \frac{1}{\gamma^2 - 1} \right] \vec{\beta} \times \vec{E} \right). \quad (10)$$

If γ is chosen so that $a_\mu - 1/(\gamma^2 - 1) = 0$ — the so-called magic γ — then \vec{E} does not affect the frequency $\vec{\omega}_a$.

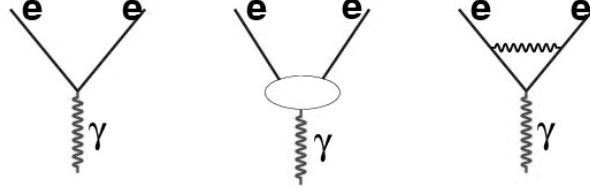


FIG. 4a. (left) Lowest-order Feynman diagram describing scattering of an electron by an external magnetic field, (middle) diagram representing an infinite set of Feynman diagrams contributing to a_e , and (right) second-order vertex diagram.

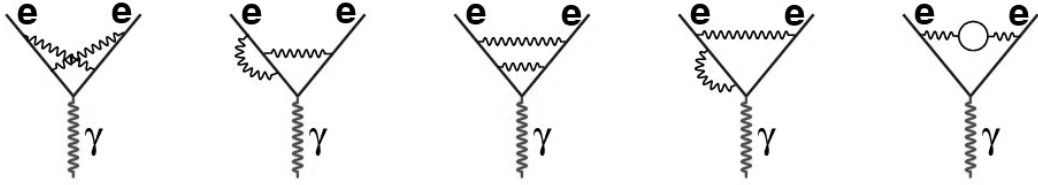


FIG. 4b. Examples of fourth-order vertex diagrams contributing to C_2 .

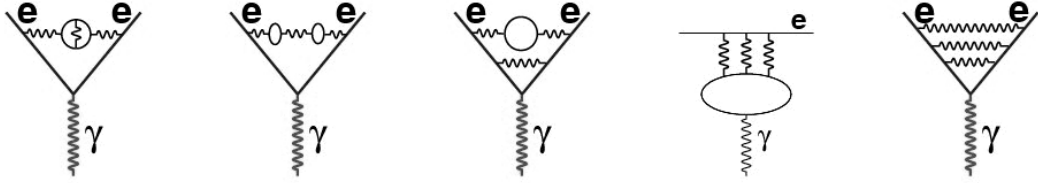


FIG. 4c. Examples of sixth-order vertex diagrams contributing to C_3 .

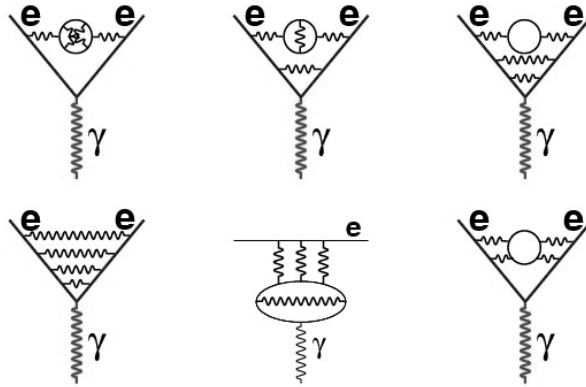


FIG. 4d. Examples of eighth-order vertex diagrams contributing to C_4 .

FIG. 4: Feynman diagrams for a_e .

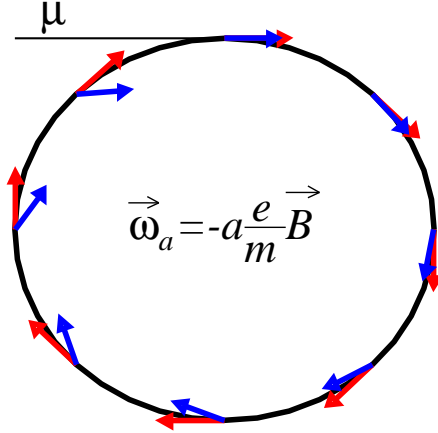


FIG. 5: Muon momentum and spin motion in an electromagnetic field. The muon spin direction is determined by detection of the decay positron.

The spin direction of the muon is determined from the direction of emission of decay positrons from muon decay, $\mu^+ \rightarrow e^+ + \nu_e + \bar{\nu}_\mu$. Parity conservation is violated in this decay so that there is a correlation between the muon spin direction and the direction of emission of the positrons. In the muon rest frame the differential transition probability for muon decay is given by

$$d\Gamma = N(E_e) \left(1 + \frac{1 - 2E_e}{3 - 2E_e} \cos \theta \right) d\Omega, \quad (11)$$

in which E_e is the positron energy in units of $m_\mu/2$, $N(E_e)$ is a normalization factor, θ is the angle between the positron motion in the muon rest frame and the muon spin direction. The factor $(1 - 2E_e)/(3 - 2E_e)$ is designated the asymmetry factor A . The μ^+ decay distribution is peaked strongly for small θ .

Decay positrons are observed by electromagnetic calorimeters. The number of decay positrons with energies greater than E emitted at time t after muons are injected into the storage ring,

$$N(t) = N_0(E) \exp \left(\frac{-t}{\gamma\tau} \right) [1 + A(E) \sin(\omega_a t + \phi(E))], \quad (12)$$

in which $N_0(E)$ is a normalization factor, τ is the muon lifetime in the muon rest frame ($\tau \simeq 2 \mu\text{s}$), and A is the asymmetry factor for positrons with energies greater than E . The exponential factor arises from muon decay and the factor in brackets accounts for the muon $g - 2$ angular frequency ω_a [24].

The angular frequency ω_a is determined from the time distribution of decay positrons observed with electromagnetic calorimeters.

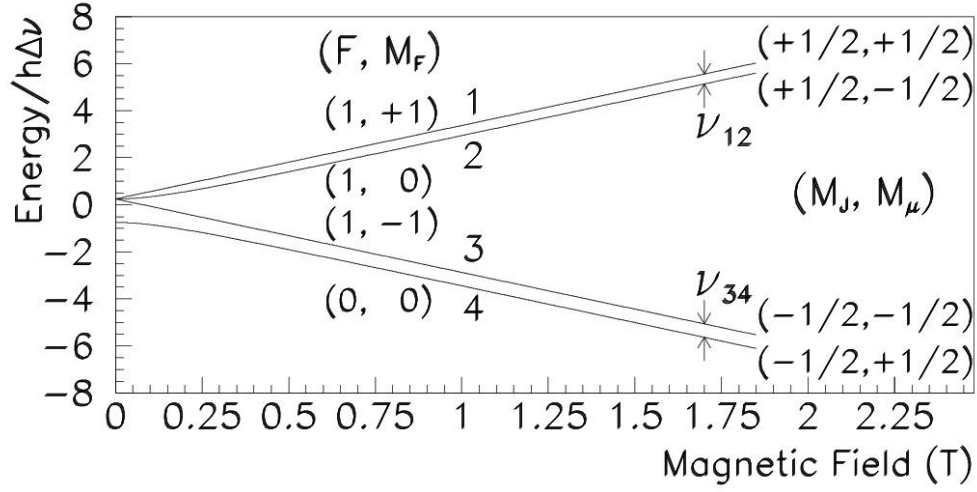


FIG. 6: Breit-Rabi energy level diagram of ground state muonium. At high fields the transitions ν_{12} and ν_{34} are essentially muon spin flip transitions.

The magnetic field B is measured by nuclear magnetic resonance (NMR) using a standard spherical probe of H_2O . This standard can be related to the magnetic moment of a free proton. Hence,

$$B = \frac{\hbar\omega_p}{2\mu_p}.$$

Using the above relation for B , the frequency ω_a from Eq. 9, and $\mu_\mu = (1 + a_\mu)e\hbar/(2m_\mu c)$, one obtains

$$a_\mu = \frac{R}{\lambda - R}, \quad (13)$$

where $R = \omega_a/\omega_p$ and $\lambda = \mu_\mu/\mu_p$.

The quantity λ appears because the value of m_μ is needed, and also because the B field measurement involves M_p . Measurements of the microwave spectrum of ground state muonium have provided a precise value for λ [25]. The hyperfine and Zeeman levels of $^2S_{1/2}$ ground state muonium are shown in Fig. 6. Microwave transitions ν_{12} and ν_{34} are measured in a strong magnetic field B of 1.6 T. The experiment utilizes the parity nonconserving correlation of the direction of the muon spin and the positron emission in the decay $\mu^+ \rightarrow e^+ + \nu_e + \bar{\nu}_\mu$.

Both the hfs interval $\Delta\nu$ and the muon magnetic moment μ_μ are determined from ν_{12} and ν_{34} ,

$$\begin{aligned} \Delta\nu &= \nu_{12} + \nu_{34}, \\ \mu_\mu B &= \nu_{34} - \nu_{12} + \Delta\nu \left(\sqrt{1 + x^2} - x \right), \end{aligned}$$

where $x = (g_J\mu_B^e + g'_\mu\mu_B^\mu)B/(h\Delta\nu)$ is proportional to the magnetic field strength. The measured value $\Delta\nu$ in combination with $\Delta\nu(\text{theory})$ [26] determine

$$\frac{\mu_\mu}{\mu_p} = \lambda = 3.183\,345\,39(10) \text{ (30 ppb) [25]}. \quad (14)$$

IV. PARTICLE DYNAMICS

Both the orbital and spin dynamics are important for the muon $g - 2$ experiment. The orbital motion can be considered separately from the spin motion because forces on the muon associated with the spin are negligible compared to the forces on the charge due to the magnetic and electric fields in the storage ring.

The force \vec{F} on a particle with charge e moving with a velocity \vec{v} in fields \vec{E} and \vec{B} is

$$\vec{F} = e \left(\vec{E} + \vec{v} \times \vec{B} \right) = \frac{d\vec{p}}{dt}. \quad (15)$$

In a uniform field \vec{B} the particle motion is circular and the equilibrium radius is

$$r_0 = \frac{E_0}{ecB_0}, \quad (16)$$

for a relativistic particle of energy E_0 moving in a field B_0 .

The relativistic equations of motion in cylindrical coordinates of a muon with charge e in a static magnetic field $\vec{B}(r, z)$ and a static electric field $\vec{E}(r, z)$ where the fields have azimuthal symmetry, i.e. are independent of θ , are [27, 28]:

$$\frac{d}{dt}(m\dot{r}) = mr\dot{\theta}^2 - er\dot{\theta}B_z + eE_r, \quad (17)$$

$$\frac{d}{dt}(mr^2\dot{\theta}) = 0, \quad (18)$$

$$\frac{d}{dt}(m\dot{z}) = er\dot{\theta}B_r + eE_z, \quad (19)$$

in which r, θ, z are the radial, azimuthal, and vertical coordinates of the particle.

The betatron oscillations are important in our experiment because they modify the positron time spectrum.

For our storage ring, the magnetic field needs to be very homogeneous and weak focusing of the muons is provided by an electric quadrupole field. Since weak focusing by an inhomogeneous magnetic field is the usual and well-understood approach, we first review focusing by an inhomogeneous magnetic field and then provide its equivalence to weak focusing by an electric quadrupole field.

For focusing by an inhomogeneous magnetic field we take:

$$B_z = B_0 \left(\frac{r_0}{r} \right)^n.$$

Hence, $\partial B_z / \partial r = -B_z n / r$. From the Maxwell equation $\nabla \times \vec{B} = 0$,

$$\frac{\partial B_z}{\partial r} = \frac{\partial B_r}{\partial z} = -\frac{n}{r} B_z \simeq -\frac{n}{r_0} B_0, \quad B_r = -\frac{n}{r_0} B_0 z,$$

in which the field index n is

$$n = \frac{-r}{B_z} \frac{\partial B_z}{\partial r}. \quad (20)$$

The equations given above with $E_r = E_z = 0$ and with $B_z = B_0(r_0/r)^n$ can be rewritten in the coordinates $x = r - r_0$, $\dot{\phi} = \dot{\theta} - \omega_0$, and $z = z$:

$$\begin{aligned} \frac{d^2 x}{dt^2} + (1 - n)\omega_0^2 x &= 0, \\ \frac{d^2 z}{dt^2} + n\omega_0^2 z &= 0. \end{aligned}$$

The solutions of these equations are:

$$x = A \cos(\sqrt{1 - n}\omega_0 t), \quad (21)$$

$$z = B \cos(\sqrt{n}\omega_0 t), \quad (22)$$

in which the amplitudes A and B depend on the initial conditions for the particle motion.

To establish the equivalence of focusing by an electric quadrupole field and of weak focusing by an inhomogeneous magnetic field we equate the focusing force due to the electric quadrupole field and that due to the inhomogeneous magnetic field,

$$eE_z = e \left(\vec{v} \times \vec{B} \right)_z = evB_r,$$

for motion in the z -direction with small displacement.

For a quadrupole electric field

$$\vec{E} = E_1(x\hat{x} + z\hat{z}), \quad \text{with } E_1 = \frac{\partial E_z}{\partial z},$$

where

$$E_1 = \frac{\partial E_z}{\partial z} = \frac{2V_0}{z_1^2},$$

in which V_0 is the electric potential on the electrode at $z = z_1$. Hence,

$$n = \frac{2V_0}{z_1^2} \frac{r_0^2}{E_0}, \quad (23)$$

in which E_0 is the particle energy. Motion in the r direction has the same n value [14]. A simple, alternative approach is to use Eq. 15. This indicates that the force due to an electric field linear in the distance from the axis (quadrupole field) will be the same as that due to a magnetic field with a spatial gradient also linear in the distance from the axis, provided that Eq. 23 holds.

The amplitude and phase of the betatron oscillations for a particle depends on its initial point in phase space at injection. The injected pulse with a width of about 50 ns and the subsequent kicker pulse of 400 ns determine the phase space of the beam at the initial time from which particle orbits are considered. The electric quadrupoles are pulsed on prior to muon injection at a lower voltage than their final voltage for a period of 20 μ s in order to eliminate muons which would otherwise not be stored (scraping) [14].

The equation of motion for the spin in its rest frame is [29–32]:

$$\frac{d\vec{s}}{dt'} = \frac{ge}{mc} \vec{s} \times \vec{B}',$$

where the primes denote quantities defined in the rest frame and \vec{s} is the spin in that frame. This is a classical equation but is the same as the quantum mechanical equation for the polarization vector [33]. Thus the relativistic equation of motion for the spin is:

$$\frac{d\vec{s}}{dt} = \frac{e}{mc} \vec{s} \times \left(\left[a + \frac{1}{\gamma} \right] \vec{B} - a \frac{\gamma}{\gamma + 1} [\vec{\beta} \cdot \vec{B}] \vec{\beta} - \left[\frac{g}{2} - \frac{\gamma}{\gamma + 1} \right] \vec{\beta} \times \vec{E} \right). \quad (24)$$

The muon spin precession frequency is

$$\vec{\omega}_s = \frac{e}{mc} \left[\frac{\vec{B}}{\gamma} - \left(\frac{1}{\gamma + 1} \right) \vec{\beta} \times \vec{E} + a_\mu (\vec{B} - \vec{\beta} \times \vec{E}) \right], \quad (25)$$

in which the fields \vec{B} and \vec{E} are the electromagnetic fields in the laboratory frame, which has a velocity $\vec{\beta}$ with respect to the muon rest frame, and $\vec{\omega}_s$ is measured in the laboratory frame. The orbital angular frequency is

$$\vec{\omega}_c = \frac{e}{mc} \left[\frac{\vec{B}}{\gamma} - \frac{\gamma}{\gamma + 1} \vec{\beta} \times \vec{E} \right]. \quad (26)$$

Hence, the difference frequency is given by:

$$\vec{\omega}_a = \vec{\omega}_s - \vec{\omega}_c = \frac{e}{mc} \left[a_\mu \vec{B} + \left(\frac{1}{\gamma^2 - 1} - a_\mu \right) \vec{\beta} \times \vec{E} \right]. \quad (27)$$

The case where $\gamma = \gamma_{\text{magic}}$ is of primary interest to us. The case in which $\gamma \neq \gamma_{\text{magic}}$ and $\vec{\beta}$ has a small component perpendicular to the plane of the orbit is associated with betatron oscillations, and is treated below.

Two small, but important, effects of the electric field \vec{E} on the spin precession frequency ω_a are first the change in ω_a when the momentum p , or γ , does not have the magic value. This effect can be represented as a change in the effective magnetic field [14],

$$B_z(\text{eff}) = B_z + \frac{E_r}{\beta} \left[\frac{1 + \frac{1}{a_\mu}}{\gamma^2} \right]. \quad (28)$$

The second effect is a pitch correction arising from the vertical betatron oscillations [34]. This correction arises if the muon has a small component of velocity v_z perpendicular to the equilibrium plane. The particle will follow a spiral path with pitch angle ψ and ω_a is altered. The focusing force due to \vec{E} changes v_z at the betatron oscillation frequency ω_z so that $\psi = \psi_0 \sin \omega_z t$. With electric field focusing and with the magic γ , the corrected value ω_a is

$$\omega'_a = \omega_a(1 - C), \quad (29)$$

in which the correction factor $C \sim 10^{-6}$ is given by

$$C = \frac{1}{4} \psi_0^2 \left[1 - \frac{\omega_a^2}{\gamma^2(\omega_a^2 - \omega_p^2)} \right]. \quad (30)$$

A mechanism for muon losses in the storage ring is that of non-linear resonances [35, 36]. Field imperfections, primarily associated with higher order moments in the electric field, or alignment errors, drive resonances in the betatron motion in single or coupled transverse degrees of freedom. This causes the amplitude of these oscillations to breathe or to grow continuously. This change in amplitude of the oscillation depends on the proximity to the resonance conditions and generally leads to muon loss from the storage ring. Such loss is minimized by a suitable choice of the field index n , in our case $n \simeq 0.137$, well away from the resonance conditions. Similarly, muon depolarization can occur due to field imperfections which affect the spin and betatron motions, and can drive resonances at the spin precession frequency.

V. EXPERIMENTAL SETUP

The experiment is done at the Brookhaven National Laboratory (BNL). It uses a secondary muon beam obtained from the primary proton beam of the Alternating Gradient Synchrotron (AGS) and a superferric storage ring.

Highly polarized μ^+ of 3.09 GeV/ c are injected through a superconducting inflector into a storage ring 14.2 m in diameter with an effective circular aperture 9 cm in diameter. The

superferric storage ring has a homogeneous magnetic field of 1.45 T, which is measured by an NMR system relative to the free proton NMR frequency. Electrostatic quadrupoles provide vertical focusing. A pulsed magnetic kicker gives a 10 mrad deflection which places the muons onto stored orbits. The muons start in 50 ns bunches and debunch with a decay time of about 20 μ s owing to their 0.6% momentum spread. Decay positrons are detected using 24 lead/scintillating fiber electromagnetic calorimeters read out by waveform digitizers. The waveform digitizer and NMR clocks were phase-locked to the Loran *C* frequency signal.

The AGS accelerator complex at BNL is shown in Fig. 7. The intense proton beam of 200 MeV from the linac is injected into a booster ring for acceleration to 1 GeV. The output beam from the booster is injected into the AGS where it is accelerated to 24 GeV. An output beam of up to 60×10^{12} protons per AGS cycle is ejected in pulses of about 50 ns with either 6 or 12 pulse bunches per AGS cycle of 2.5 s.

An areal photograph of the BNL accelerator complex (Fig. 8) shows the AGS, the relativistic heavy ion accelerator (RHIC) and the relatively small muon storage ring. A photograph of the muon storage ring indicating also some associated equipment, is shown in Fig. 9.

The beamline to the muon storage ring is shown in Fig. 10. The proton beam from the AGS with 60×10^{12} protons per AGS cycle impinges on a nickel target of one interaction length. Either 6 or 12 pulses per AGS cycle are used with the interval between pulses being 33 ms.

The 3.1 GeV/ c positive muon beam was formed from decays of a secondary pion beam which was 1.7% higher in momentum, thus providing a muon polarization of about 95%. The beamline consists of dipole, quadrupole and sextapole magnets. The pion decay channel is a 72 m long straight section of the secondary beamline. The muons were selected at a momentum slit, where the (higher energy) pions were directed into a beam dump. The beam composition at the entrance to the storage ring was measured with a threshold Čerenkov counter filled with isobutane. By stepping the pressure from zero to 1.2 atm, the thresholds for Čerenkov light from e^+ , then μ^+ , and finally π^+ were crossed. The beam was found to consist of equal parts of positrons, muons and pions, consistent with Monte Carlo predictions. While this measurement was not sensitive to the proton content of the beam, calculations predict it to be approximately one third of the pion flux. The flux incident on the storage ring was typically 2×10^6 for each proton pulse.

The transverse beam emittance is matched with four quadrupoles just upstream in the beamline of the $g - 2$ storage ring to allow passage into the storage ring through the back leg of the ring magnet and the inflector described below.

A superconducting inflector magnet [37] 1.7 m in length placed between the hole in the

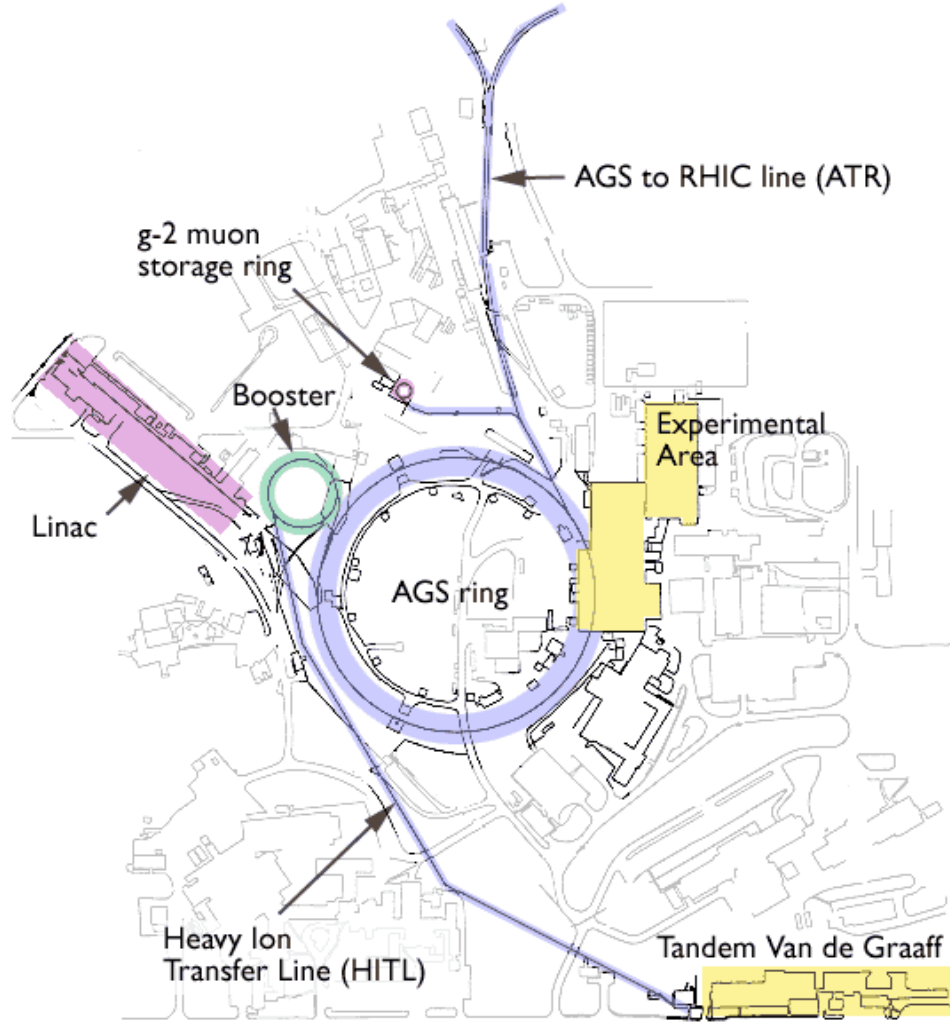


FIG. 7: Schematic overview of the AGS complex at BNL.

back of the yoke and the edge of the muon storage region substantially cancels the 1.45 T storage-ring field and delivers the beam approximately parallel to the central orbit but 77 mm farther out in radius (Fig. 11). The inflector aperture of $18(w) \times 57(h)$ mm² is necessarily smaller than the storage aperture of 90 mm diameter, so that the Twiss parameters of the incoming beam do not match those of the ring.

The 10 mrad kick (Fig. 12) needed to put the muon beam onto a stable orbit was achieved with a peak current of 4100 A and a half period of 400 ns. Three pulse-forming networks powered three identical 1.7 m long one-loop kicker sections consisting of 95 mm high parallel plates on either side of the beam. The current pulse was formed by an under-damped LCR circuit. The kicker plate geometry and composition were chosen to minimize eddy currents.

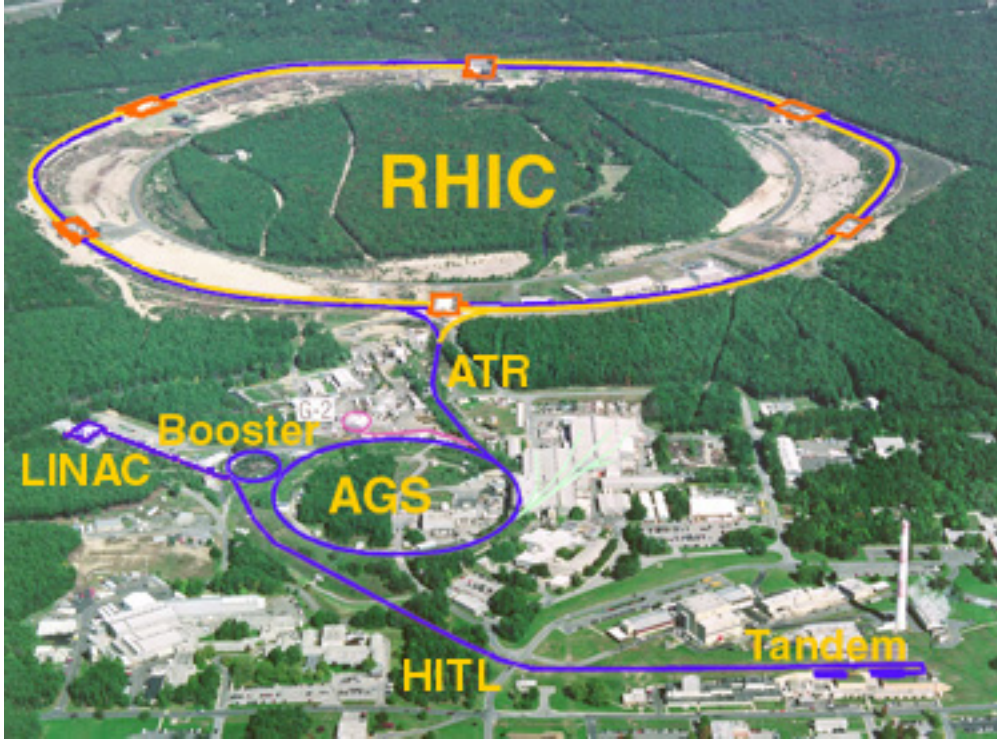


FIG. 8: Areal photograph of the BNL accelerator complex.

The maximum additional field seen by the muons in a kicker region was 0.017 T. Some $20 \mu\text{s}$ after the kicker pulse, the local residual field due to eddy currents is seen to be smaller than $\sim 1 \times 10^{-6}$ T, which corresponds to less than 0.1 ppm on the global field. The time-varying magnetic field from the eddy currents was calculated with the program OPERA and was measured in a full-size straight prototype vacuum chamber with the use of the Faraday effect. Since the muons circulate in 149 ns, they were kicked several times before the kicker pulse died out.

The magnetic field in the storage ring must be determined at the sub ppm level (~ 0.1 ppm), so the storage ring field must have high homogeneity and stability. The super-ferric magnet [38] is constructed of iron with superconducting coils. Construction tolerances of 1 mm are achieved for our 14 m diameter storage ring (Fig. 13).

High quality steel is used and in particular for the pole pieces ultra-low-carbon steel is employed. The opening between the pole faces is 18 cm and the active storage region is 9 cm in diameter. Wedge-shaped openings between the pole faces and the return yoke allow the insertion of wedge-shaped iron shims in the gaps. The openings between the pole pieces and the return yoke help to decouple the field in the gap from the imperfections in the yoke iron

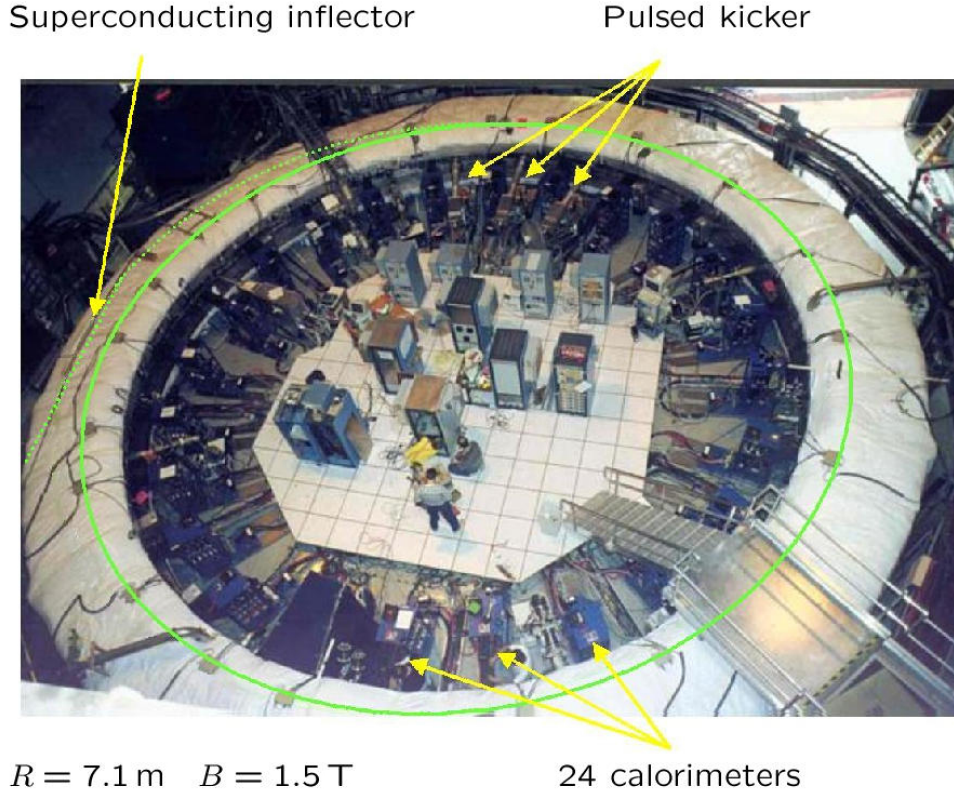


FIG. 9: The E821 muon storage ring.

such as pot holes and inhomogeneities of the iron.

The magnet is excited by three NbTi/Cu superconducting coils which are 14.2 m in diameter and carry 5200 A. A low-voltage high-current power supply with a current stability of 0.3 ppm is used. Feedback to the power supply from the NMR field measurements maintains the field to 0.1 ppm.

Extensive provisions for shimming include large iron pieces around the yoke, iron shimming wedges, edge shims, several types of correcting coils on the surface of the pole pieces, and iron shims on the pole pieces near regions where the poles meet. The shimming wedges affect principally the dipole and quadrupole components of the field, whereas the edge shims affect the sextupole components.

Features of the magnetic field measurement are shown in Fig. 14. A pulsed NMR system is used and a free induction decay is shown [39]. The Fourier spectrum is centered at 62 MHz ($B = 1.45 \text{ T}$) with a width of 40 Hz, so the NMR frequency is measured to 0.1 ppm.

The magnetic field along the muon trajectory in the active volume of the storage ring

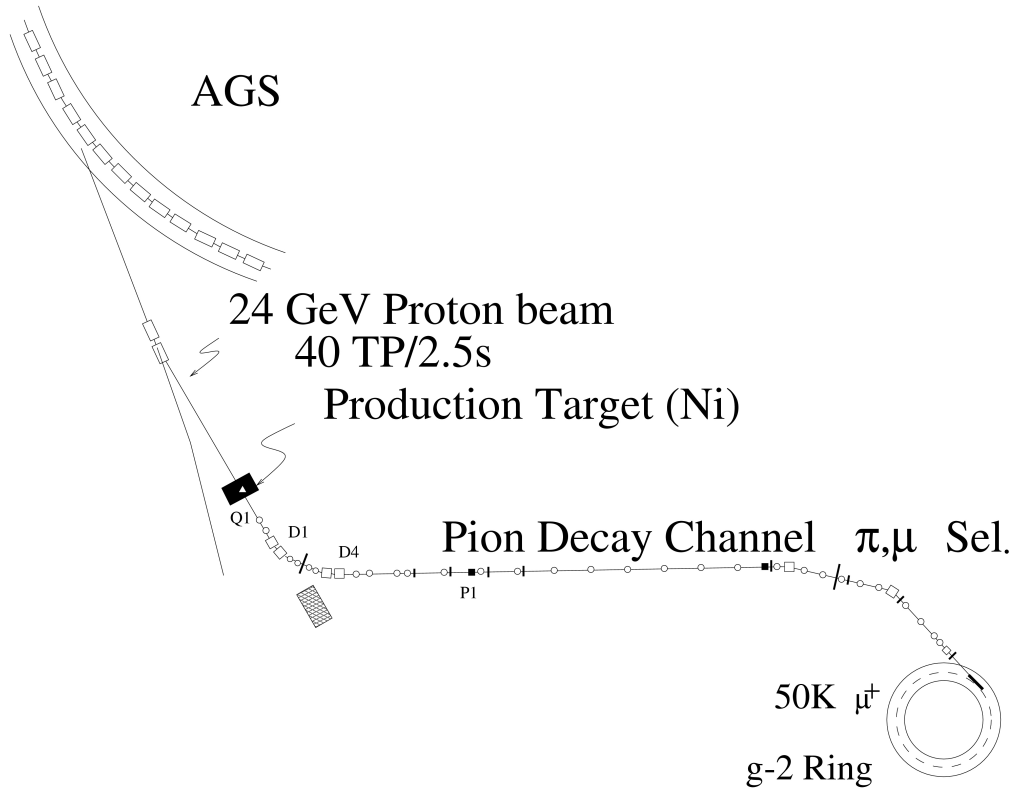


FIG. 10: Schematic overview of the beamline to the muon storage ring.

is measured by 17 NMR paraffin probes mounted on a trolley which is pulled through the vacuum chamber of the storage ring by a cable car mechanism [40]. The electronics for the NMR system is contained within the trolley. The trolley traverses the ring in about 2 hrs and obtains some 50,000 NMR readings. A trolley run is taken every 2 or 3 days. Some 375 NMR probes are embedded in the top and bottom walls of the aluminum vacuum chamber and the field is measured continuously by these fixed probes. The average of some 100 of these probes is used as a feedback signal to the power supply for the superconducting coils. The trolley probes are calibrated against a standard probe before and after data-taking with the muon beam. The data are written to disk for off-line analysis.

Results of magnetic field measurements are shown in Fig. 15. The field measured with the center probe on the trolley is plotted versus the azimuthal angle and is seen to be uniform to about ± 50 ppm. The exception is a region of about 1° near the superconducting inflector where its fringe field changes the field by about 600 ppm. A new inflector was installed after 1999 which did not have this fringe field. The average radial field component was measured

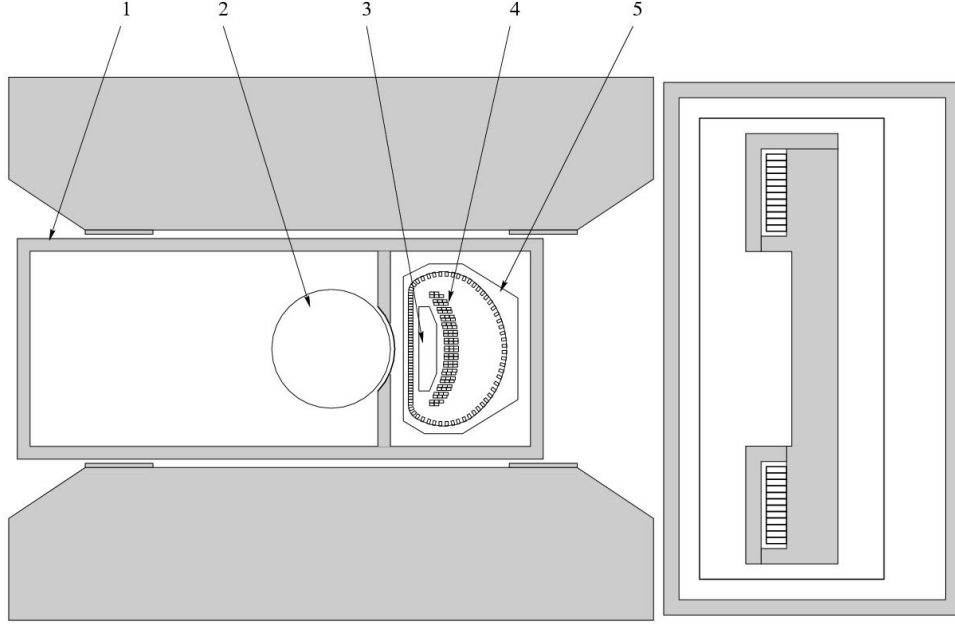


FIG. 11: Cross sectional view of the inflector magnet at the injection into the ring. Shown are (1) the storage vacuum chamber wall, (2) the muon storage region, (3) the inflector channel, (4) the superconducting coils, and (5) the inflector casing.

using Hall probes and found to be less than 50 ppm of the vertical field value [41].

The 17 trolley probe measurements obtained in a complete trolley revolution are used to evaluate the average azimuthal field which is expressed in terms of its multipoles with B_0 being the dipole field determined to about 0.1 ppm. Contours of equal B are shown with 1 ppm levels with respect to B_0 indicating that the azimuthal average field varies by only a few ppm over the cross section of the storage ring. The field average of the fixed probes with respect to a reference field obtained from trolley runs is shown versus time. Fig. 15d shows the perturbation of the NMR reading of a single fixed probe caused by the trolley as it passes by.

Calibration of the trolley probes with respect to our standard probe is necessary to obtain finally the field in units of the free proton NMR frequency. Our standard probe (Fig. 16) is a spherical water sample carefully constructed to contain a 1 cm^3 spherical water sample and to be well insulated from environmental perturbations [42]. The diamagnetic shielding factor σ given by

$$B_p = (1 - \sigma)B_{spherwater}$$

has been measured in a separate experiment [43] which measured $g_p(\text{H}_2\text{O})/g_J(\text{H})$ and a

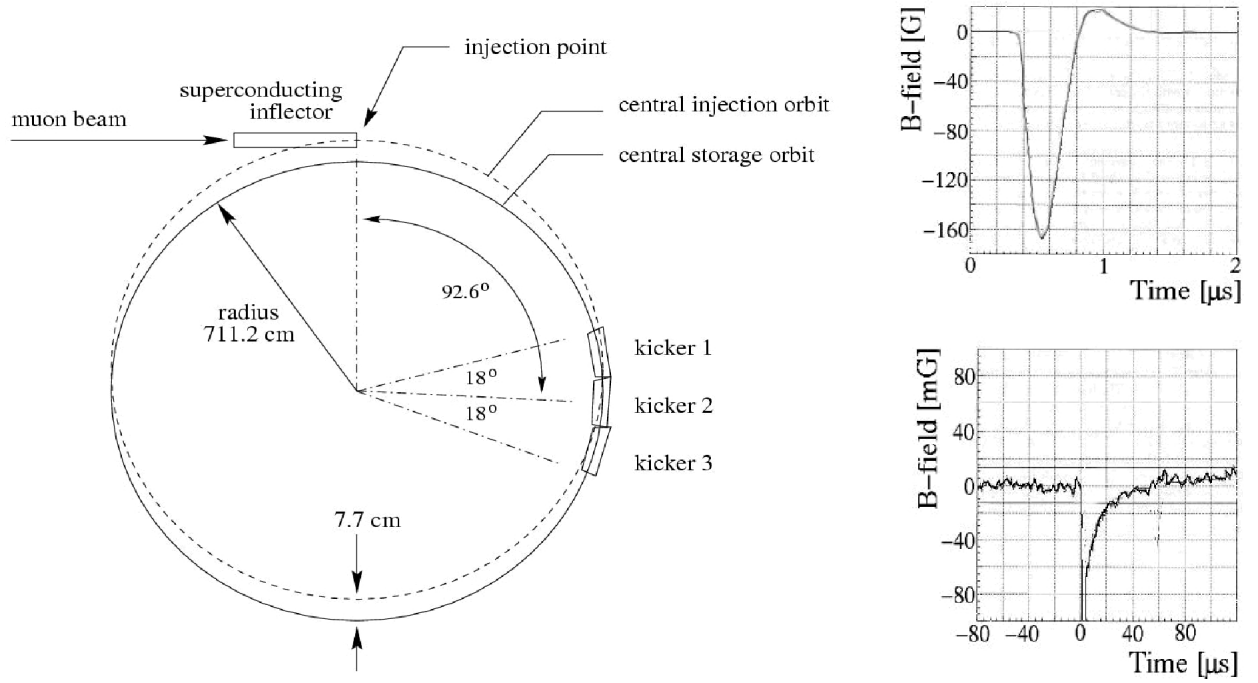


FIG. 12: The schematics of muon injection and storage in the $g-2$ ring (left) and the measured changes in the field B when the kicker is fired (right).

second which used a hydrogen maser to measure $g_J(\text{H})/g_p(\text{H})$ [44]. In addition, a theoretical calculation of $g_p(\text{H})/g_p$ is required [45, 46]. These give

$$\begin{aligned} \frac{g_J(\text{H})}{g_p(\text{H}_2\text{O})} &= -658.216\,009\,1(69), \\ \frac{g_J(\text{H})}{g_p(\text{H})} &= -658.210\,706(6), \text{ and} \\ \frac{g_p(\text{H})}{g_p} &= 1 - 17.733 \cdot 10^{-6}. \end{aligned}$$

Hence,

$$\sigma(\text{H}_2\text{O}) = 25.790(14) \times 10^{-6} \text{ at } 34.7^\circ\text{C} [43],$$

which includes the calculable shielding for a proton in atomic hydrogen, $\sigma = 17.733$ ppm [45, 46]. The temperature dependence of $\sigma_{\text{H}_2\text{O}}$ is measured to be $10.36(30)$ ppb/ $^\circ\text{C}$ [47].

The ideal electric quadrupole field required for vertical focusing of the muon beam is shown in Fig. 17a. Fig. 17b shows a cross sectional view of the actual electrode configuration consisting of rectangular plates. There are four electric quadrupole sections around the ring, each covering about 40° in azimuth. The electrodes are powered on for about 1 ms starting

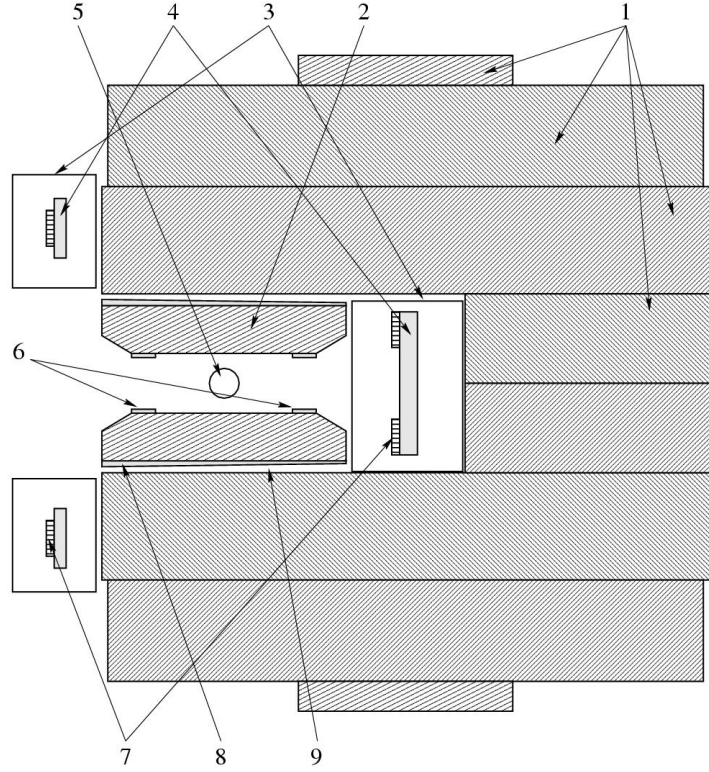
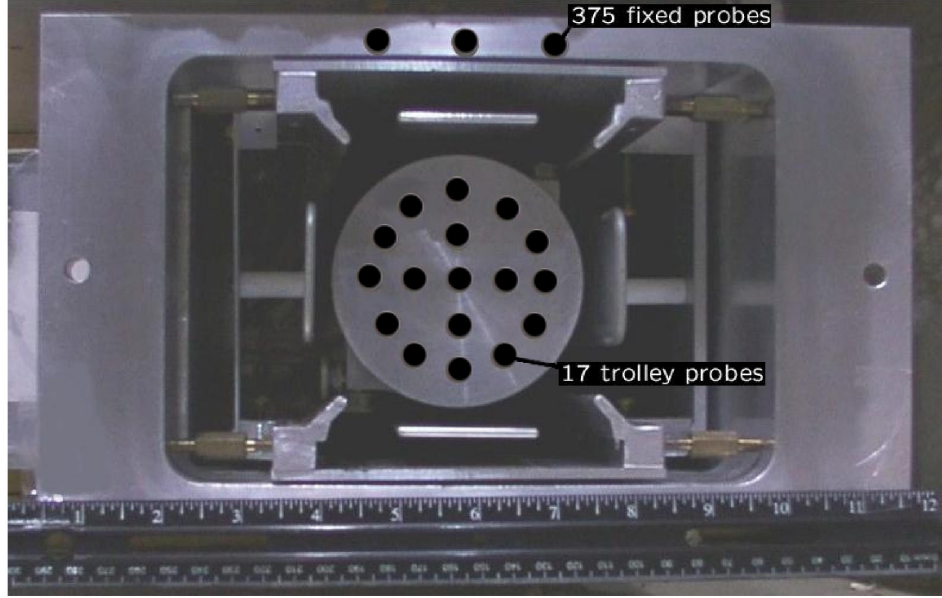


FIG. 13: Cross sectional view of the C magnet. Shown are (1) the yoke plates, (2) the pole tips, (3) the cryostat, (4) the mandrels, (5) the muon storage region, (6) the edge shims, (7) the superconducting coils, (8) the wedge shims, and (9) the air gap. The magnet opening faces towards the ring center.

shortly before each beam pulse and then turned off to avoid electrical breakdown. The nominal electrode voltages are ± 24 kV. However, for about $15 \mu\text{s}$ following muon injection, two of the electrodes are kept at lower voltages of ± 17 kV to steer the outer region of the beam onto collimators inside the storage ring. This procedure, called scraping, removes muons from the ring which could otherwise be lost in an uncontrolled manner during our measurement time.

The stored muon beam, its position, width, and oscillatory motion in its dependence on the kicker and quadrupole settings, is measured several times during the running period with scintillating fibers that can be plunged into the storage region at two locations. Indirect measurements of the beam position and width are provided by horizontal scintillation fingers mounted on the front-face of five positron calorimeters, described below. The front scintillation counters are used in addition in determining muon beam losses.

Positrons from the in-flight decay $\mu^+ \rightarrow e^+ \nu_e \bar{\nu}_\mu$ are detected with lead/scintillating fiber



Free induction decay signals:

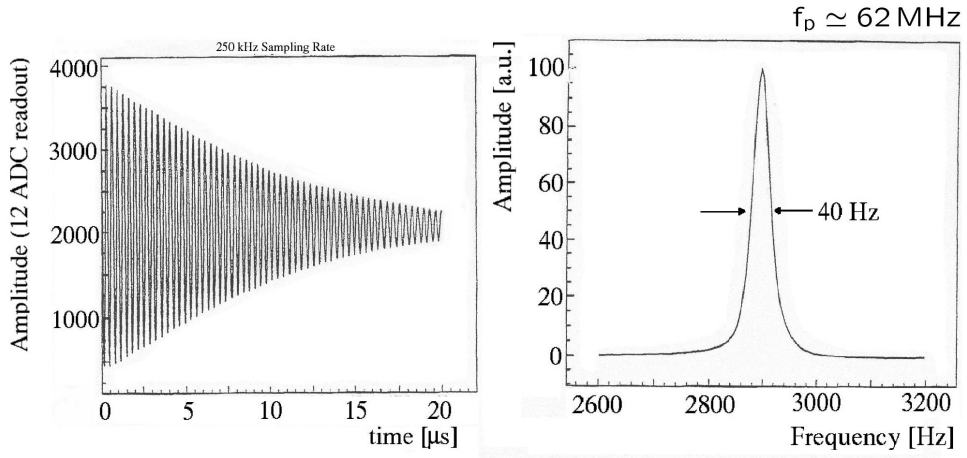


FIG. 14: The field trolley inside the storage region (top) and the free induction decay signal (bottom).

calorimeters [48] placed symmetrically at 24 positions around the inside of the storage ring (Fig. 18). The electromagnetic calorimeters are connected by light guides to four fast and stable photomultipliers, and the signals are added. The calorimeter has a good energy resolution ($\sigma/E = 10\%$ at 1 GeV) and the scalloped vacuum chamber minimizes preshowering before the positrons reach the calorimeters. Fig. 18 shows a typical pulse with a width of

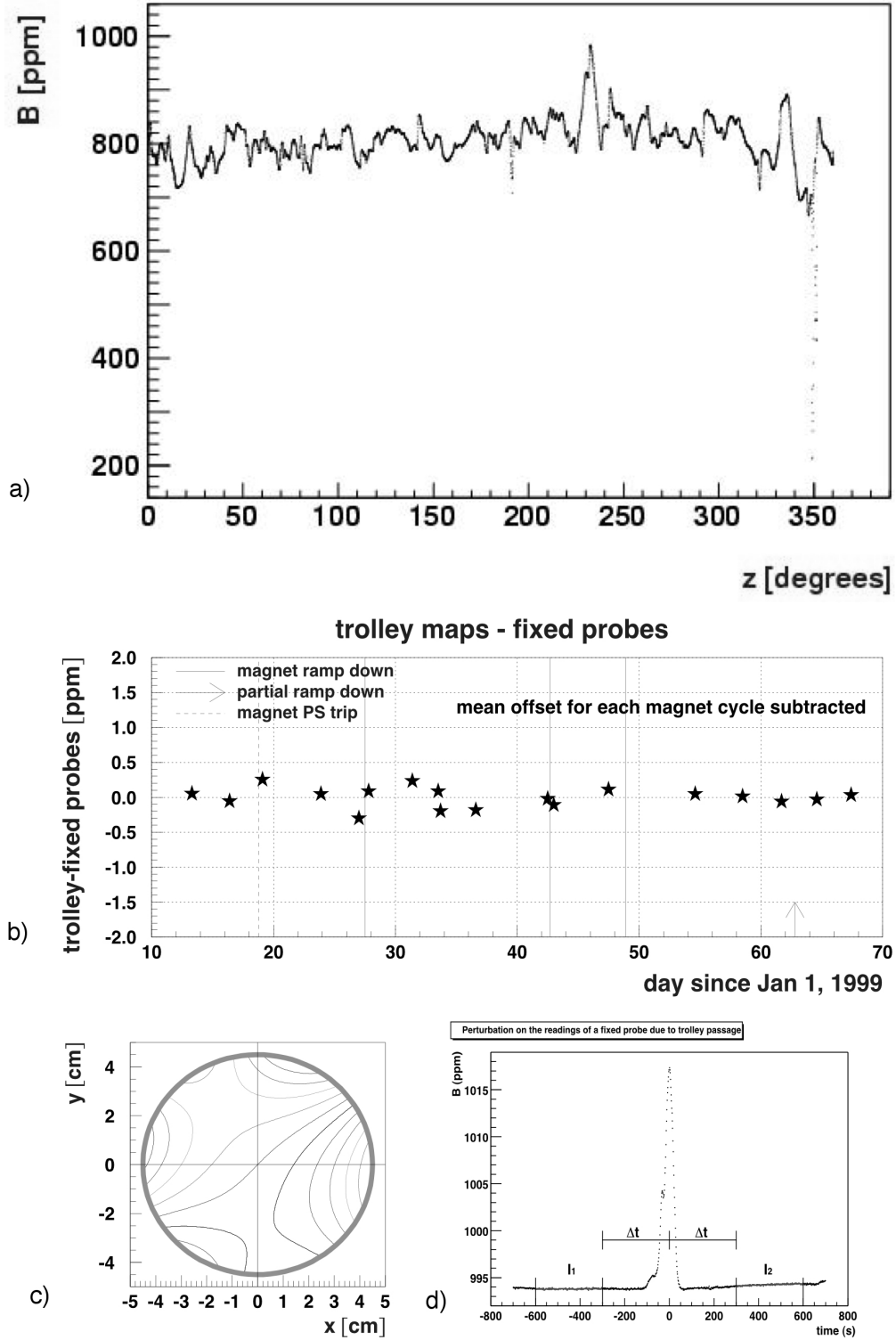


FIG. 15: a) The magnetic field measured with the trolley center probe versus azimuth from measurements taken on February 5, 1999. The dip at 350° results from the inflector fringe field. The field values are expressed in ppm with respect to a central azimuthal average field $B_0 = 1.451\,266\,\text{T}$. b) Field tracking with the fixed probes, as described in the text. c) Multipole expansion of the field averaged over azimuth. The contour lines are 1 ppm contour lines. d) The perturbation of a fixed probe reading as the trolley passes by.

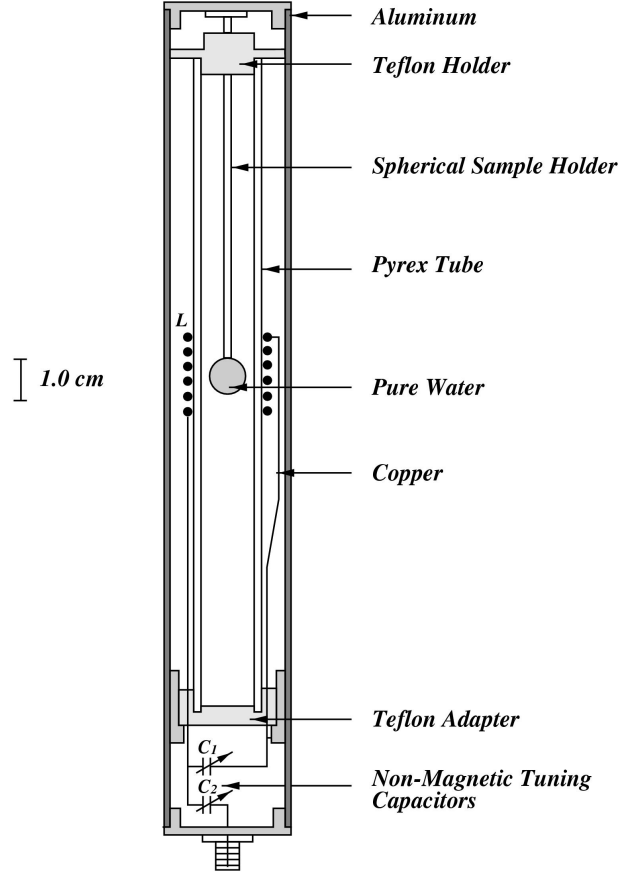


FIG. 16: The reference probe used in the $g - 2$ field measurements.

about 20 ns and also shows a succession of pulses during a $55 \mu\text{s}$ time interval. For each signal its time and energy is determined in the off-line analysis. To a good approximation the decay positron time spectrum is described by

$$N(t) = N_0(E) \exp\left(\frac{-t}{\gamma\tau}\right) [1 + A(E) \sin(\omega_a t + \phi(E))], \quad (31)$$

in which the normalization $N_0(E)$ and the parity violating asymmetry parameter $A(E)$ depend strongly on the energy threshold E . The dependence of the phase $\phi(E)$ results from the E dependence of the measured positron detection times relative to the muon decay times, and is much weaker. The hardware energy threshold is set to about 1 GeV.

The photomultiplier tubes of the calorimeter were gated off before injection, and when gated on, they recovered to 90% pulse height in ≤ 400 ns and reached full operating gain in several μs . The early data until about $10 \mu\text{s}$ were used in the off-line analysis to determine

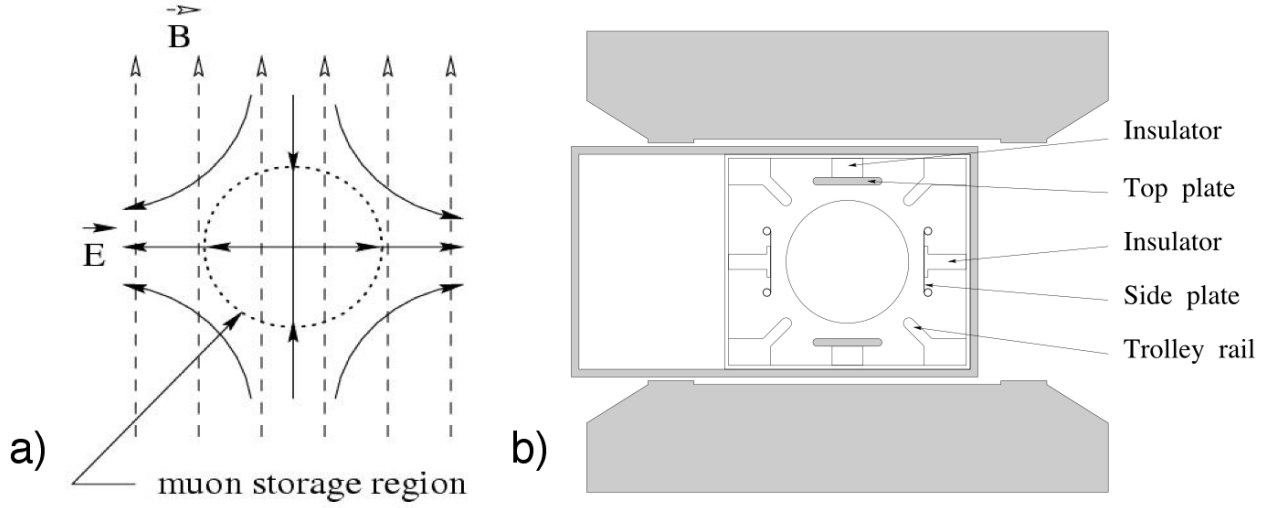


FIG. 17: Illustration of electrostatic focusing in the $g - 2$ experiment.

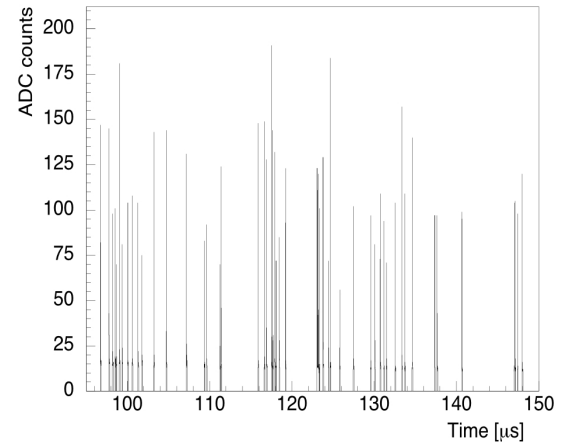
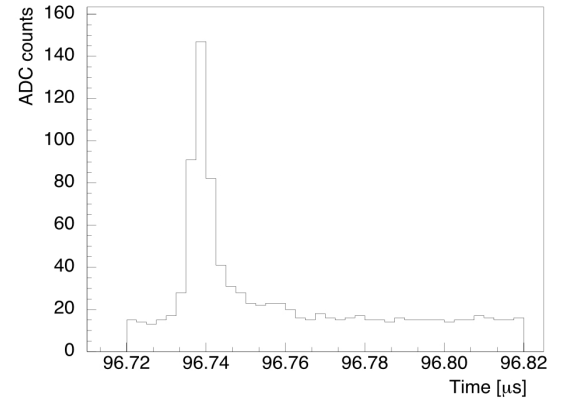


FIG. 18: One of the 24 positron calorimeters in the $g - 2$ experiment (left), together with event displays of the signal shapes recorded with the waveform digitizers for two time scales (right).

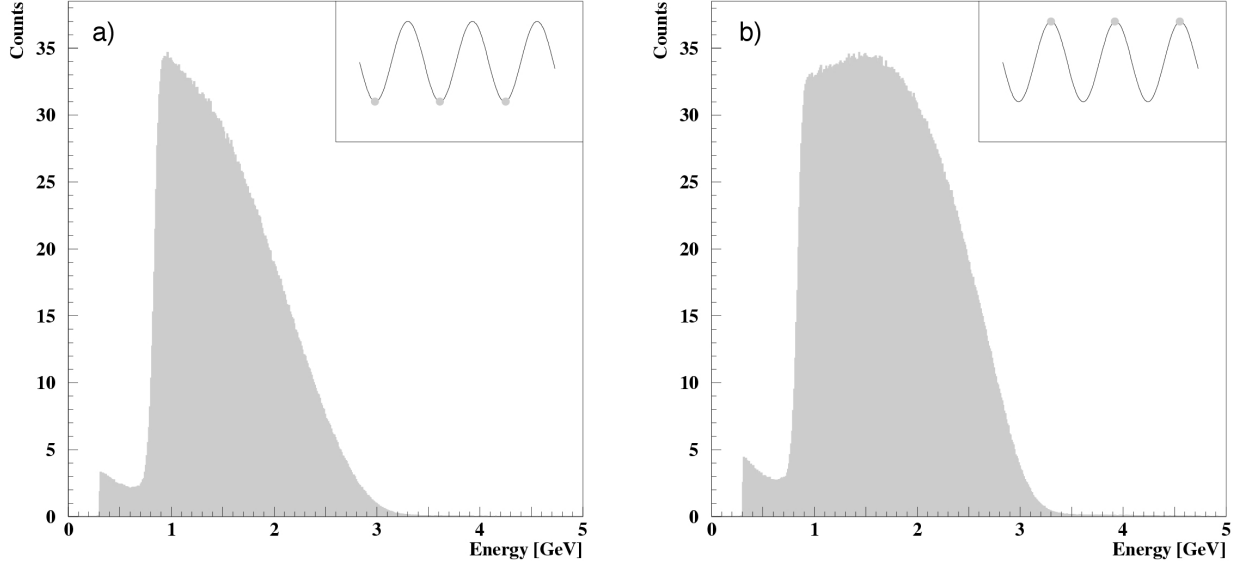


FIG. 19: Observed decay positron energy spectra a) when the muon spins predominantly oppose the muon momenta and b) when the spins are along the momenta. The corresponding $g-2$ phases are illustrated in the insets.

the muon rotation frequencies. The detector gains were constant 25–40 μs after injection. Data were accumulated for about 10 muon lifetimes following injection.

The calorimeter pulses were continuously sampled by custom 400 MHz waveform digitizers (WFDs) — similar to the subsequent design of Ref. [49] — which record at least 16 8-bit samples (2.5 ns each) on both the fast rising and slower tail of the positron pulse, and thus provide both timing and energy information. The NMR and WFD clocks were phase-locked to the same LORAN-C [50] frequency signal. The waveforms were zero-suppressed and stored in buffer memories until the end of the AGS cycle. Between AGS acceleration cycles the data were written to tape for off-line analysis, as were the calorimeter calibration data.

A laser/LED (light-emitting diode) calibration system was used to monitor calorimeter time and gain shifts during the data-collection period. Early-to-late timing shifts over the first 200 μs were, on average, less than 20 ps. Phototube gain shifts were determined from the off-line e^+ energy spectrum to be less than 0.3% from 32 μs on.

Positron energy spectra are shown in Fig. 19. For a single detector and single positron the maximum energy is 3.1 GeV. Higher energy signals are due to detection resolution and overlapping pulses. The difference in the energy spectra when the spin direction is pointed towards and away from the detector is owing to the muon decay characteristics.

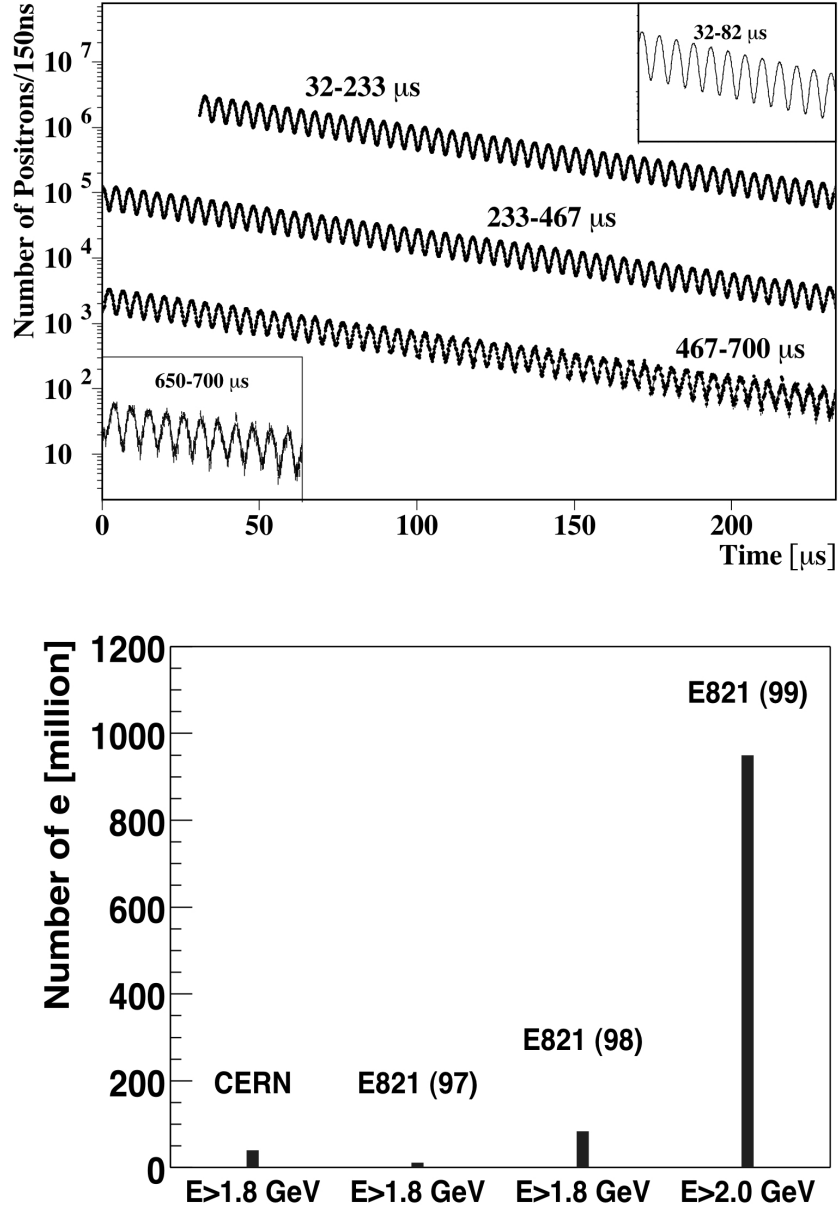


FIG. 20: Time spectrum for the $1 \cdot 10^9$ analyzed e^+ with energies larger than 2 GeV together with the fitted function discussed in the text (top) and a comparison of the number of analyzed positrons for the results published to date (bottom).

A positron time spectrum is shown in Fig. 20 from a starting time of 32 μs to 700 μs . The exponential decay with the muon dilated lifetime of about 64 μs as well as the modulation with the $g - 2$ frequency of about 230 kHz are evident. The data were acquired in sequences of about 30 minutes, so called runs, during about 500 hours of the two month running period

in the winter of 1999. The total number of positron counts obtained in the CERN experiment and in the three BNL data-taking periods are shown in Fig. 20.

VI. DATA ANALYSIS

The analysis of a_μ follows, naturally, the separation of the measurement in the frequency ω_p related to the magnetic field and the frequency ω_a related to the muon spin precession,

$$a_\mu = \frac{R}{\lambda - R}, \quad (32)$$

where $R = \omega_a/\omega_p$ and $\lambda = 3.183\,345\,39(10)$ (30 ppb) [25] is taken from external measurements and theory. The analyses of ω_p and ω_a have both been performed by several largely independent groups within the muon ($g-2$) collaboration. Only after each of the analyses had been finalized were the results for ω_p and ω_a from the various analyses combined, and was the value of a_μ evaluated. At no earlier stage was the value of a_μ or R known to any of the collaborators.

In the following, we choose to describe one analysis of ω_p and one analysis of ω_a in some detail, followed by a short overview of the differences with other analyses and a discussion of their results. It should be noted that, at the pursued precision, both the analysis of ω_p and the analysis of ω_a are intricate enough to have taken well over a year to complete. Only aspects are reviewed here.

A. The analysis of ω_p

The analysis of the 1999 magnetic field data starts with the calibration of the NMR probes in the field trolley from measurements taken at the beginning and end of the 1999 running period. In these measurements, the field in the storage ring is tuned to very good homogeneity at specific calibration locations. Its value is then measured with the 17 NMR probes mounted in the trolley shell, after which the trolley is moved out of the way. A single probe is then plunged into the storage vacuum and positioned to measure the 17 field values corresponding to the same spatial configuration as the trolley probes (cf. Fig 14). The difference of the trolley probe readings and the plunging probe readings forms a calibration of the trolley probes with respect to the plunging probe, and hence with respect to each other. Drifts of the field during the calibration are determined by remeasuring the field with the trolley following the measurements with the plunging probe, and also using the readings from nearby NMR probes in the outer top and bottom walls of the vacuum chamber. The plunging probe, as well as a select subset of trolley probes, are thereafter calibrated in

air against our standard probe [42] using a similar sequence of measurements. The series of calibration measurements were made by several collaborators independently. The leading calibration uncertainties result from the residual inhomogeneity of the field at the calibration locations, and from position uncertainties in the active volumes of the NMR probes. The uncertainties in the azimuthal direction were estimated from measurements in which the trolley shell was purposely displaced. The uncertainties in the radial and vertical directions were estimated by comparison of trolley and plunging probe measurements during which a known and relatively large sextupole field of about 7 ppm at $r_0 = 4.5$ cm was applied using the surface correction coils. Their total is estimated to be 0.2 ppm, as indicated in Table I. The dependencies of the trolley NMR readings on the supply voltage and on other settings, as well as the dependence on the temperature inside the trolley shell, were measured to be small in the range of operation. The combined upper limits are included as a systematic uncertainty ("other"), which also includes the effects from the measured transient kicker field caused by eddy currents (Fig. 12). The uncertainty in the absolute calibration of the standard probe amounts to 0.05 ppm.

The magnetic field inside the storage region was measured 17 times with the field trolley during the data collection from January to March 1999. Fig. 15a shows the field value measured with the center trolley probe in the storage ring versus the azimuthal angle. Fig. 15c shows a multipole expansion of the azimuthal averages of readings from all probes,

$$B_y = \sum_{n=0}^{\infty} C_n r^n \cos(n\phi) - \sum_{n=0}^{\infty} D_n r^n \sin(n\phi), \quad (33)$$

$$B_x = \sum_{n=0}^{\infty} C_n r^n \sin(n\phi) + \sum_{n=0}^{\infty} D_n r^n \cos(n\phi), \quad (34)$$

where the coefficients C_n and D_n are the normal and skew multipoles, respectively. The dipole term C_0 dominates the other multipoles, because of the field uniformity. In the analysis, terms up to and including $n = 4$ — the decupoles — are kept. Dedicated measurements with probes extending to the full beam aperture of 4.5 cm radius — 1.0 cm beyond the outer trolley probes — show that the neglect of higher multipoles is at most 0.03 ppm in terms of the average field encountered by the stored beam muons, thus confirming design calculations. The field in azimuth is seen to be uniform to within about 50 ppm, except for a region of about 1° near 350° , where the inflector magnet is located. An imperfection in its superconducting shield resulted in a residual fringe field, which reduces the storage ring central field by about 600 ppm up to 3000 ppm at the edge of the aperture. Consequently, in this region not all 17 NMR probes in the trolley could be operated with their nominal settings, and the field had to be measured in separate scans with the field trolley. The uncertainty associated

with matching the measurements in the narrow inflector region with the measurements in the storage ring is estimated to be 0.2 ppm. Uncertainties, or more precisely non-linearities, in the determination of the trolley position during the measurements — from the measured cable lengths and from perturbations on the readings from fixed probes as the trolley passes — affect the azimuthal average of the field at the level of 0.1 ppm.

The measurements with the field trolley serve, in addition, as a calibration of the 375 NMR probes in the outer top and bottom walls of the storage vacuum chamber, the so called fixed probes, which are used to track the field when the field trolley is 'parked' in the storage vacuum just outside the beam region, and muons circulate in the storage ring (cf. Fig 14). A representative probe reading when the field trolley passes by is shown Fig. 15d. The calibration for each fixed probe consists in determining the difference between the trolley measurement of the field at the azimuthal location of the fixed probe and the fixed probe readings, interpolated so as to cancel the perturbing effects of the trolley shell and electronics. The calibration may change in time, for example when the magnet is ramped or when the settings of surface correction coils are modified. Hence, field measurements with the trolley are made whenever ramping of the magnet or a change in settings requires such, and repeated typically two to three times per week. A weighted average of the readings of the fixed probes is formed in a way so as to optimize the correlation with the determination of the azimuthal average of the dipole field B_0 measured with the field trolley. Fig. 15b shows the scatter of the difference of the determinations of B_0 from measurements with the fixed probes and with the trolley probes. The scatter of about 0.2 ppm of the differences in periods of constant settings and magnet powering is a measure of the uncertainty in the field tracking with the fixed probes.

The field frequency ω_p in Eq. 32 is the free proton NMR frequency averaged over the muon distribution and over the analyzed data sample. The field integral encountered by the muon beam has been studied by tracking 4000 muons for 100 turns through a measured field map. The simulation shows that the value of the field integral over the beam trajectory is identical to within 0.05 ppm to the azimuthally averaged field value, taken at the beam center. The beam center along the radial axis is determined by analyzing the debunching of the beam pulses [24], and found to be 3.7(1.0) mm outside of the central orbit. The vertical beam center is determined to be 2(2) mm above the center plane from measurements with the front scintillation counters and scintillating fibers mentioned before in Section V.

The resulting value for the field frequency ω_p is,

$$\omega_p = 61\,719\,256(25) \text{ Hz} \quad (0.4 \text{ ppm}), \quad (35)$$

where the uncertainty has leading contributions from the calibration of the trolley probes

TABLE I: Systematic errors for the ω_p analysis

Source of errors	Size [ppm]
1. Standard probe absolute calibration	0.05
2. Calibration of B_0 against standard probe	0.20
3. B_{aver} from trolley probes due to position uncertainty	0.10
4. Inflector fringe field	0.20
5. Tracking by fixed probes	0.15
6. Average over muon distribution	0.12
7. Others \dagger	0.15
Total systematic error on ω_p	0.4

\dagger higher multipoles, trolley temperature and its power supply voltage response, and eddy currents from the kicker.

and the inflector fringe field (cf. Table I), and is thus predominantly systematic. A second, largely independent, analysis of the field has been conducted, using a different selection of fixed NMR probes among other differences. The results agree for each trolley measurement to within 0.05 ppm and to within 0.03 ppm for the frequency ω_p in Eq. 35.

B. The analysis of ω_a

The determination of the frequency ω_a from the recorded calorimeter WFD traces proceeds in stages.

In the initial stage, the WFD traces are scanned to identify positron pulses and to measure their properties. Conceptually, a sample of about 10^4 pulses in the energy range of 1–3 GeV is selected for each calorimeter individually to form an average pulshape, which is then used in fits to all WFD traces. The selection is made from recordings well after the muons were injected into the ring, so as to ensure that transient effects have faded away and the traces consist of responses to single positrons. Fig. 21 shows the average pulshape for one of the positron calorimeters (left) together with its application to a typical WFD trace (right). The algorithm is seen to assign an appropriate pedestal for the trace, to identify the single positron pulse, and to fit its peak value (energy) and location (time). A fraction of several percent of the recordings is found to contain multiple positron pulses per WFD trace. Extensive studies of the pulse finding and fitting algorithm show that in such cases each of the pulses is identified and measured correctly, provided that the pulse separation

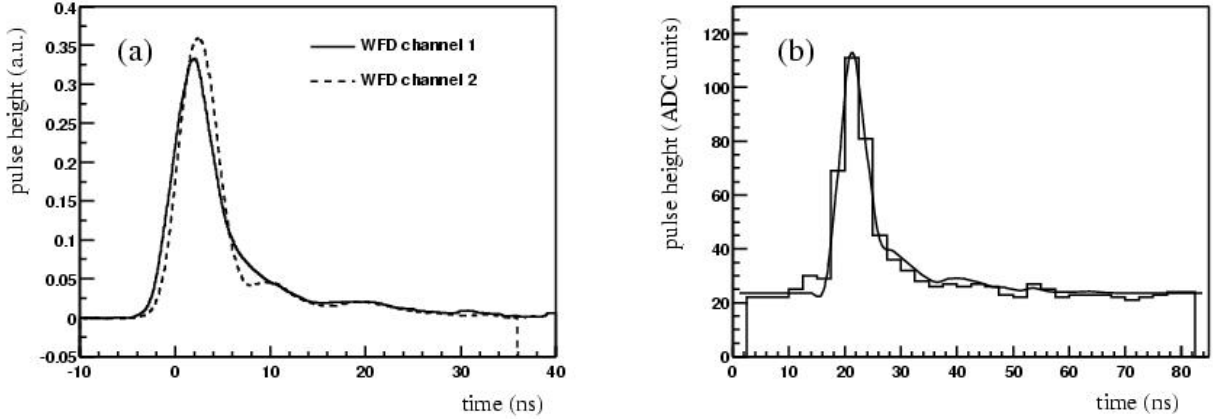


FIG. 21: The average response to a single positron pulse in the energy range of 1–3 GeV for both WFD readout phases (a) and (b) its application to a typical pulse.

exceeds 3 ns and the pulse energy is larger than 0.4 GeV. For intervals smaller than 3 ns, the pulses are reconstructed as a single pulse, whereas pulses with energies below 0.4 GeV escape reconstruction. The studies of the algorithm show, furthermore, that time shifts of the positron reconstruction chain are smaller than 20 ps over 200 μ s, so that time shifts contribute less than 0.1 ppm systematic uncertainty in the frequency ω_a .

In the subsequent analysis stage, the data collected to study systematic effects are separated from the data with regular running conditions. Data for which the settings of the apparatus are known to be different from their nominal values are rejected, as are data for which the correspondence could be established. Data recorded during occasional mishappenings are of course discarded as well. The consistency of the remaining data is verified with a variant [51] of the Kolmogorov-Smirnov test, in which the (integral) positron time-energy spectra for each data run are compared with a reference spectrum created by randomly sampled events from all runs. Per construction, this test is *insensitive* to oscillations in the spectra and therefore does not bias the sample available for further analysis of ω_a .

The time spectrum of the remaining positrons is shown in Fig. 20 in the time range 32–700 μ s and for positron energies larger than 2 GeV. Corrections were applied to mask the bunched time structure of the beam injection and to eliminate a small distortion from overlapping pulses, so called pileup. The key characteristics of the spectrum arise from muon decay and spin precession, and are described by:

$$N(t) = N_0(E) \exp\left(\frac{-t}{\gamma\tau}\right) [1 + A(E) \sin(\omega_a t + \phi(E))], \quad (36)$$

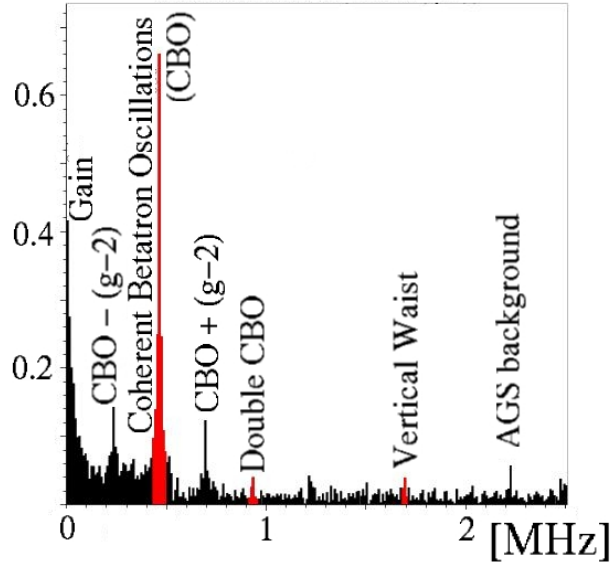


FIG. 22: Fourier transform of residuals of fit to the 1999 data-taking into account muon decay and spin precession.

in which $N_0(E)$ is the normalization, $A(E)$ the asymmetry, and $\phi(E)$ the phase, as before (cf. Eq. 12). The statistical uncertainty on the frequency ω_a from a fit with a function $f(t) = N(t)$ to the time spectrum is inversely proportional to $A\sqrt{N_E}$ with N_E the total number of positrons in the spectrum with energies larger than E , and has its optimal value for $E \simeq 2$ GeV. The optimal value amounts to 5 ppm for the $84 \cdot 10^6$ analyzed positrons from the 1998 data [52], which are described adequately with this function.

The tenfold larger positron sample collected in 1999 requires consideration of additional effects, as evidenced from the Fourier transform of residuals in Fig. 22 from a fit $f(t) = N(t)$ to the 1999 data. We discuss several of these effects — coherent betatron oscillations, muon losses, detector gain changes, and AGS background — after describing the corrections to the data for pileup and for beam debunching mentioned before.

- The number of overlapping pulses in the reconstructed data is proportional to the instantaneous counting rate squared $(dN/dt)^2$ and to the minimum pulse separation time of the pulse reconstruction algorithm. This fraction is about 1% of the event sample at $32 \mu\text{s}$ when the fits of ω_a to the data are started, and vanishes exponentially with a time constant equal to half the dilated muon lifetime. Pileup distorts the positron time spectrum because of miscounting of the number of pulses and misidentification of the energies and times. Since the phase ϕ in Eq. 12 depends on the positron energy

and correlates strongly with the frequency ω_a in fits, pileup potentially causes a sizable error in the fitted value of ω_a . It is thus advantageous to apply a correction to the data prior to the fitting, which consists in a subtraction of a pileup spectrum that is constructed using indiscriminately recorded pulses as follows. Positron pulses found within a window at a fixed, short time after the positron pulse that triggered the WFD module are treated as if they overlap with the trigger pulse, that is, the times of both pulses are averaged and the energies added to form a single pulse. The width of the window is taken equal to the minimum pulse separation time of 3 ns. For data with energies above 2 GeV — twice the hardware threshold of about 1 GeV — the difference of the thus found spectrum and the uncorrected spectrum determines the pileup spectrum. The difference spectrum has both negative and positive entries, since pulses may be lost by combination as well as gained when pulses each with energies below the software threshold (2 GeV) are combined to form a single pulse with sufficient energy to pass the threshold.

Signals with energies below about 0.4 GeV are too small to be reconstructed with the pulse finding algorithm and are thus not accounted for in the subtraction procedure described above. These small signals distort the pulse reconstruction but do not, on average, affect the energy. They do cause small time dependent shifts in the asymmetry $A(E)$, and to a smaller extent in the phase $\phi(E)$. The observed stability of the asymmetry $A(E)$ with time is used to set a limit on the shift of the fitted value of ω_a that would result through its correlation with $\phi(E)$.

Fig. 19 shows the spectrum prior to the correction for pileup and the agreement between the positron energy spectrum after the pileup correction has been applied and the spectrum well after beam injection when the instantaneous rates are low and pileup is negligible. The inset illustrates that the average energy after pileup subtraction is constant with time, as expected. Expressed in terms of a shift in ω_a , the size of the correction for pileup amounts to 0.3 ppm. Its uncertainty is estimated to be about twice smaller.

- The injection of the beam in narrow bunches into the storage ring results in a strong modulation of the initial part of the decay positron time spectrum with the cyclotron period of 149.185 ns. This effect is, in fact, used to determine the equilibrium beam radius. The modulation fades with a characteristic time of about 24 μ s owing to the 0.6% momentum spread in the beam. Since the fits of ω_a are started as early as 32 μ s after beam injection, a correction to the data is necessary. An effective correction is found to consist in randomization of the arrival times of all decay positrons from a

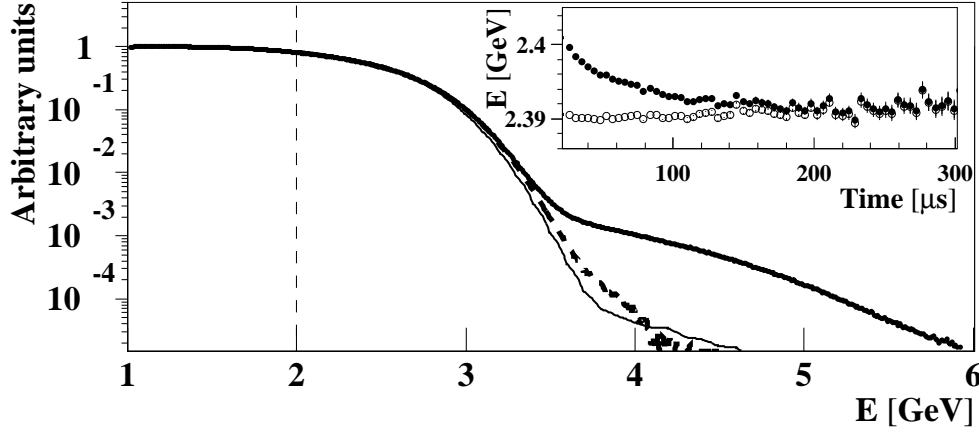


FIG. 23: Energy spectrum of all reconstructed positrons (thick line), together with the energy spectrum well after beam injection when the instantaneous rates are low and pileup is negligible (thin line) and the energy spectrum after the correction for pileup (dashed line). The inset shows the energy averaged over the $g - 2$ period versus time before (filled circles) and after (open circles) the correction for pileup has been applied.

single beam pulse over the cyclotron period, which in addition is chosen to be the bin-width of the fitted spectra.

- Coherent betatron oscillations: The storage ring is a weak focusing spectrometer with field index $n = 0.137$, with an aperture that is large compared to the inflector aperture of $18(w) \times 57(h)$ mm². Therefore, the phase space for the betatron oscillations defined by the acceptance of the storage ring is not filled when muons are injected into the storage ring [53]. In combination with imperfect injection angles and an imperfect horizontal kick to store the muons onto stable orbits, this results in betatron oscillations of the beam as a whole – coherent betatron oscillations (CBO).

The existence of these oscillations is readily appreciated from the Fourier transform in Fig. 22. The oscillations of the beam center and of the beam width have also been observed directly in dependence of the settings for the focusing quadrupoles and the kick after injection, using scintillating fiber monitors plunged into the storage region at two locations in the ring. The CBO modulate the positron time spectra, since the calorimeter acceptances depend on the muon decay positions. The dominant effect is caused by the horizontal oscillations, which decay with a characteristic time of ~ 120 μ s. An adequate parametrization of the effect is found to be

$$b(t) = 1 + A_b \exp\left(-\frac{t^2}{\tau_b^2}\right) \cos(\omega_b t + \phi_b), \quad (37)$$

and is included multiplicatively in the function fit to the data, $f(t) = N(t) \cdot b(t)$. The frequency $\omega_b = \omega_c(1 - \sqrt{1 - n}) \simeq 470.0$ kHz, with $n \simeq 0.137$ the field focusing index and ω_c the cyclotron frequency, is determined from the Fourier spectrum in Fig. 22 and measured directly several times during the running period using scintillating fibers that can be plunged into the storage region. The amplitude A_b is determined from the fit and found to be about $A_b \simeq 1 \times 10^{-2}$, as is the characteristic time $\tau_b \simeq 120 \mu\text{s}$ with which CBO vanish, owing partly to the momentum spread in the beam. The phase ϕ_b varies by detector, from 0 to 2π .

- Muon Losses: A small fraction of the stored beam is lost during the muon storage time, despite controlled scraping of the injected muon beam with the electrostatic quadrupoles for about $15 \mu\text{s}$ immediately following injection. An adequate parametrization of the residual losses is found to be

$$l(t) = 1 + n_l \exp\left(-\frac{t}{\tau_l}\right), \quad (38)$$

and is included multiplicatively in the function fit to the data, $f(t) = N(t) \cdot b(t) \cdot l(t)$. The decay time τ_l is found to be $\tau_l \simeq 20 \mu\text{s}$, and n_l is typically less than 1%. An independent study of the losses of stored beam was made using coincident signals from three adjacent layers of scintillation fingers mounted on the front faces of five of the positron calorimeters, in the absence of energy deposits in the calorimeters.

- Detector gain changes are determined using the positron energy spectra, and monitored with a pulsed laser system. The gains of all but two detectors are constant to within 0.1% over the muon storage time of about $600 \mu\text{s}$, which causes an estimated uncertainty of 0.02 ppm in the measurement of ω_a .
- AGS background: Imperfect proton extraction from the AGS sometimes causes particles to enter the storage ring during the $\sim 600 \mu\text{s}$ data collection period. These particles, mostly positrons, may cause background pulses in the calorimeters, which then contaminate the regular data sample. The time structure of such a background is defined by the AGS cyclotron period of $2.694 \mu\text{s}$, and its number distribution among the calorimeters is characteristic of the energy [54]. Both properties have been used to estimate the relative contamination to be $\simeq 10^{-4}$ for the 1999 data sample. Simulations show that this corresponds to a systematic uncertainty of 0.1 ppm in ω_a .

The function fitted to the 1999 data sample is thus given by

$$f(t) = N(t) \cdot b(t) \cdot l(t), \quad (39)$$

in which $N(t)$ describes muon decay and spin precession (cf. Eq. 12), and the perturbations $b(t)$ and $l(t)$ are given in Eqs. 37 and 38. The function $f(t)$ has ten parameters that are fit to the data, in the sense of minimizing χ^2 . (The frequency ω_b is determined from a Fourier analysis, as mentioned before.) Fig. 20 demonstrates the good agreement of data and fit, as evidenced also from the value $\chi^2 = 3819$ for the 3799 degrees of freedom (dof). The frequency ω_a is determined with a statistical precision of 1.3 ppm from the 1999 data. The fitted value of ω_a correlates weakly with all free parameters, except for the phase ϕ_a , and is thus insensitive in particular to the functional forms and values of the perturbations $b(t)$ and $l(t)$.

The internal consistency of the fit results was verified in several ways. Fig. 24 shows two examples; (top) the variation of the fitted frequency ω_a versus the time at which the fit is started, and (bottom) the fitted frequency from data of each detector individually. The values are consistent with each other ($\chi^2/\text{dof} = 30/21$) and their average equals the fit result from the data combined to within 0.07 ppm. The fitted lifetime, after correcting for muon losses, is in agreement with the value expected from special relativity to within 0.1% of the value.

Three analyses of ω_a , alternative to the one just described, were made, as mentioned before. Two of these analyses made use of data processed with an independent implementation of the pulse finding and fitting algorithm. Other principal differences concern a somewhat different choice of data selection and fitting parameters, a refined treatment of detector gain changes, and alternative ways to handle pileup. In one analysis, a pileup correction to the data is made by varying the minimum pulse separation time in the reconstruction algorithm and by extrapolating to the case of no minimum separation time (hence, vanishing pileup), whereas in another analysis pileup is incorporated in the fitted function, using the constructed pileup spectrum only to determine the associated phase. In the last analysis, the data are randomly split in four samples n_1 – n_4 which are rejoined in $u(t) = n_1(t) + n_2(t)$, $v(t) = n_3(t - \tau_a/2) + n_4(t + \tau_a/2)$, and the ratio [55]

$$r(t) = \frac{u(t) - v(t)}{u(t) + v(t)} = A(E) \sin(\omega_a t + \phi_a(E)) + \epsilon, \quad (40)$$

where τ_a is an estimate of the $g - 2$ period and the constant $\epsilon \ll 1$. The ratio $r(t)$ is largely independent of effects with time scales exceeding τ_a , particularly the muon lifetime, and can thus be fit with fewer free parameters. Its results have somewhat different systematic uncertainties. Extensive further detail on two of the alternative analyses can be found in Refs. [56] and [57].

The results from the four analyses of ω_a are found to agree to within the statistical variation of 0.4 ppm expected from the use of slightly different data reconstructions and

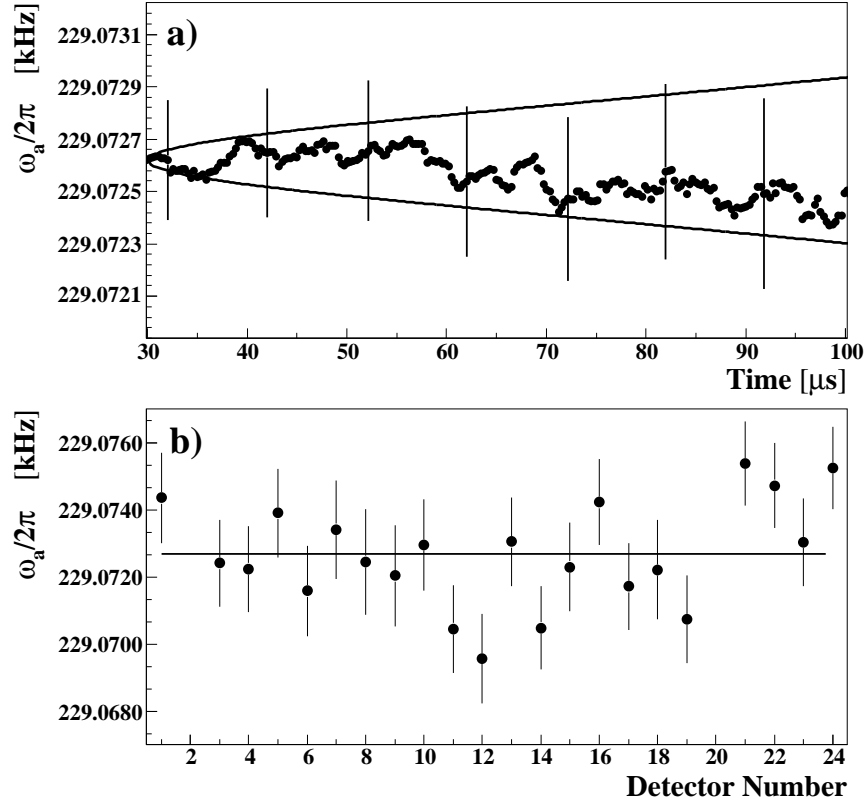


FIG. 24: a) The fitted frequency $\omega_a/(2\pi)$ versus the time after beam injection when the fit is started. The size of the statistical uncertainty is indicated for several of the points. The band indicates the size of expected statistical fluctuations. Both indicate 68% confidence intervals. b) Fits to the spectra from individual detectors. Detector 2 was excluded from analysis because of a readout problem. Detector 20 is located downstream of an array of tracking chambers; it has been excluded from analysis because of its different energy response.

selections in the respective analyses. The combined result is

$$\omega_a/2\pi = 229\,072.8(0.3) \text{ Hz (1.3 ppm)}, \quad (41)$$

which includes a correction of $+0.81(8)$ ppm for the small disproportionality of the observed frequency and the measured field caused by vertical betatron oscillations and electric fields in the storage ring (cf. Eqs. 24). The stated error of 1.3 ppm reflects the total uncertainty, accounts for the strong correlations between the individual fit results, and is dominated by the statistical contribution. The systematic uncertainties are listed in Table II. Uncertainties due to spin resonances, the fit start time, and clock synchronization were neglected after each was estimated to be less than 0.01 ppm.

TABLE II: Systematic errors for the ω_a analysis.

Source of errors	Size [ppm]
Pileup	0.13
AGS background	0.10
Lost muons	0.10
Timing shifts	0.10
E field and vertical betatron oscillation	0.08
Binning and fitting procedure	0.07
Coherent betatron oscillation	0.05
Beam debunching/randomization	0.04
Gain changes	0.02
Total systematic error on ω_a	0.3

VII. RESULTS

Only after the analyses of the magnetic field data and of the spin precession data had been finalized, separately and independently, was the anomalous magnetic moment a_μ^+ evaluated,

$$a_\mu^+ = \frac{R}{\lambda - R},$$

where $R = \omega_a/\omega_p$ and $\lambda = \mu_\mu/\mu_p = 3.183\,345\,39(10)$ [25]. The result [58],

$$a_\mu^+(\text{expt}) = 11\,659\,202(14)(6) \times 10^{-10} \quad (1.3 \text{ ppm}), \quad (42)$$

is in good agreement with previous measurements of a_μ^+ and a_μ^- [14, 24, 52] and improves the combined uncertainty by a factor of about three (Fig. 25).

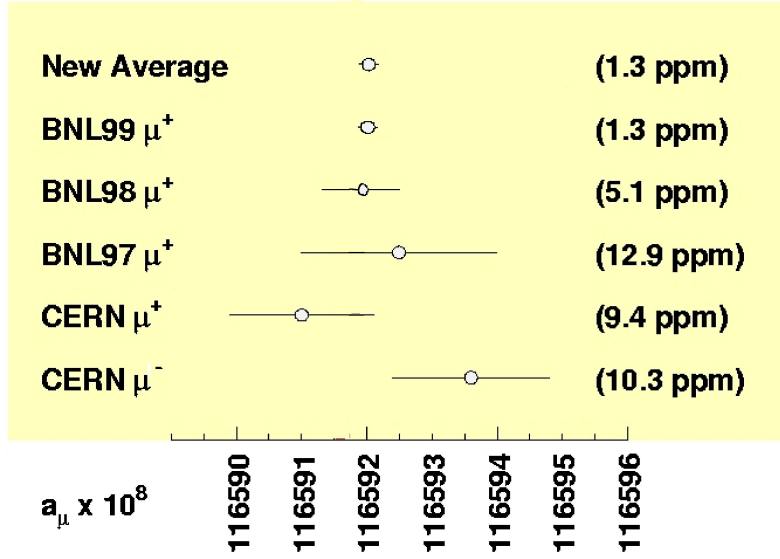
VIII. THEORETICAL VALUE FOR a_μ

The theoretical value for a_μ in the Standard Model can be written [59]

$$a_\mu(\text{SM}) = a_\mu(\text{QED}) + a_\mu(\text{had}) + a_\mu(\text{weak}). \quad (43)$$

A. QED contribution

The contribution of the electromagnetic interaction, $a_\mu(\text{QED})$, includes those of the photon, electron, muon and tauon fields as in Fig. 26. The result is most conveniently expressed

FIG. 25: Measurements of a_μ and their total uncertainties.

as [60]

$$a_\mu - a_e = A_2 \left(\frac{m_\mu}{m_e} \right) + A_2 \left(\frac{m_\mu}{m_\tau} \right) + A_3 \left(\frac{m_\mu}{m_e}, \frac{m_\mu}{m_\tau} \right).$$

The fourth order term

$$A_2^4 \left(\frac{m_\mu}{m_e} \right) \left(\frac{\alpha}{\pi} \right)^2 + A_2^4 \left(\frac{m_\mu}{m_\tau} \right) \left(\frac{\alpha}{\pi} \right)^2 = 1.094\,258\,282\,8(98) \left(\frac{\alpha}{\pi} \right)^2 + 0.000\,078\,059(25) \left(\frac{\alpha}{\pi} \right)^2.$$

$$A_2^6 \left(\frac{m_\mu}{m_e} \right) \left(\frac{\alpha}{\pi} \right)^3 + A_2^6 \left(\frac{m_\mu}{m_\tau} \right) \left(\frac{\alpha}{\pi} \right)^3 + A_3^6 \left(\frac{m_\mu}{m_e}, \frac{m_\mu}{m_\tau} \right) \left(\frac{\alpha}{\pi} \right)^3 =$$

$$22.868\,379\,36(23) \left(\frac{\alpha}{\pi} \right)^3 + 0.000\,360\,54(21) \left(\frac{\alpha}{\pi} \right)^3 + 0.000\,527\,63(17) \left(\frac{\alpha}{\pi} \right)^3.$$

$$A_2^8 \left(\frac{m_\mu}{m_e} \right) \left(\frac{\alpha}{\pi} \right)^4 + A_2^8 \left(\frac{m_\mu}{m_\tau} \right) \left(\frac{\alpha}{\pi} \right)^4 + A_3^8 \left(\frac{m_\mu}{m_e}, \frac{m_\mu}{m_\tau} \right) \left(\frac{\alpha}{\pi} \right)^4 =$$

$$127.50(41) \left(\frac{\alpha}{\pi} \right)^4 + 0 \left(\frac{\alpha}{\pi} \right)^4 + 0.079(3) \left(\frac{\alpha}{\pi} \right)^4.$$

$$A_2^{10} \left(\frac{m_\mu}{m_e} \right) \left(\frac{\alpha}{\pi} \right)^5 = 930(170) \left(\frac{\alpha}{\pi} \right)^5.$$

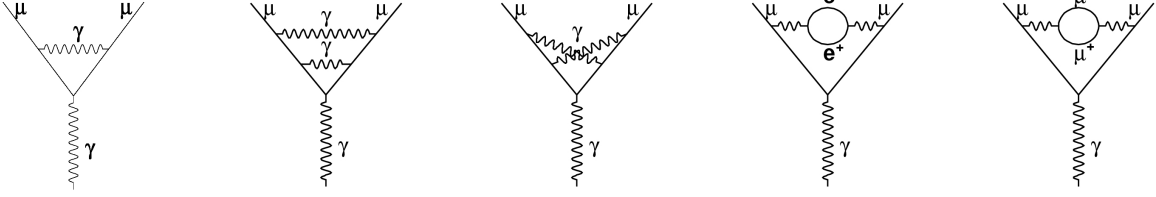


FIG. 26: Feynman diagrams of QED processes contributing to the difference of a_μ and a_e .

Hence,

$$a_\mu(\text{QED}) = 0.5 \left(\frac{\alpha}{\pi} \right) + 0.765\,857\,376(27) \left(\frac{\alpha}{\pi} \right)^2 + 24.050\,508\,98(44) \left(\frac{\alpha}{\pi} \right)^3 + 126.07(41) \left(\frac{\alpha}{\pi} \right)^4 + 930(170) \left(\frac{\alpha}{\pi} \right)^5, \quad (44)$$

where the uncertainties originate from the uncertainties in the mass ratios, and for terms of order higher than $(\alpha/\pi)^3$ from numerical evaluation. Substituting the $\alpha^{-1}(a_e)$ value from Eq. 6 one obtains [20, 59]:

$$a_\mu(\text{QED}) = 11\,658\,470.57(29) \times 10^{-10} \quad (25 \text{ ppb}). \quad (45)$$

A substantially improved evaluation of the higher order term $A_2^8(m_\mu/m_e)$ to reduce round-off or digit deficiency is in progress [61]. It is interesting to note that the contribution of the tau lepton through modifying the photon propagator amounts to 4×10^{-10} or 0.36 ppm.

B. Hadronic Contribution

The hadronic contribution to a_μ is about 60 ppm, and contributes the principal uncertainty to $a_\mu(\text{SM})$. It arises in lowest order as a vacuum polarization correction involving virtual hadrons as shown in Figure 28a.

This diagram can not now be calculated from QCD. However, by dispersion theory this contribution can be related to $R(s) = \sigma_{\text{total}}(e^+e^- \rightarrow \text{hadrons})/\sigma_{\text{total}}(e^+e^- \rightarrow \mu^+\mu^-)$, in which s is the square of the total energy in the center of mass for the colliding particles e^+, e^- . The dispersion relation,

$$a_\mu(\text{had } 1) = \left(\frac{\alpha m_\mu}{3\pi} \right)^2 \int_{4m_\pi^2}^{\infty} \frac{ds}{s^2} K(s) R(s), \quad (46)$$

involves the integral from the threshold energy for pion pair production to ∞ and contains the $1/s^2$ factor as well as the kinematic factor $K(s)$, which increases monotonically to 1 as

$s \rightarrow \infty$,

$$K(s) = x^2 \left(1 - \frac{x^2}{2}\right) + \frac{1+x}{1-x} x^2 \ln x + (1+x)^2 \left(1 + \frac{1}{x^2}\right) \left(\ln(1+x) - x + \frac{x^2}{2}\right),$$

where

$$x = \frac{1 - \sqrt{1 - \frac{4m_\mu^2}{s}}}{1 + \sqrt{1 - \frac{4m_\mu^2}{s}}}.$$

The value for $a_\mu(\text{had } 1)$ is evaluated from the dispersion integral with measured values of R . Data from hadronic τ^- decay can also be used, assuming the validity of isospin symmetry and conservation of the vector current (CVC).

The principal contribution to $a_\mu(\text{had } 1)$ comes from the region below $\sqrt{s} = 1$ GeV. Extensive and accurate measurements of R have been made and are continuing at the Budker Institute of Nuclear Physics in Novosibirsk in the energy range for $\sqrt{s} = 0.3 - 1.4$ GeV, using VEPP-2M and their CMD-2 detector. Their older measurements have provided the principal data for evaluation of $a_\mu(\text{had } 1)$ [62] and their much more recent and extensive data around the ρ -meson have been published [63]. The full data set is also being analyzed for the energy regions $\sqrt{s} = 370\text{--}540$ MeV and $\sqrt{s} = 1040\text{--}1380$ MeV. The upgraded VEPP-2M collider in Novosibirsk (VEPP-2000) will extend the energy range up to 2 GeV. New measurements of R are also being obtained with the e^+e^- collider in Beijing in the approximate energy range $\sqrt{s} = 2\text{--}5$ GeV [64], and are also expected from the new Frascati ϕ factory. Extensive data on hadronic τ^- decay come from LEP [65, 66] and Cornell [67], and can be expected from the B factories.

The measured spectral function of the $\tau^- \rightarrow \pi^- \pi^0 \nu_\tau$ decay can be used in addition to evaluate $a_\mu(\text{had } 1)$, assuming CVC and isospin symmetry [68]. Detailed measurements of τ^- decay are provided by ALEPH [65], OPAL [66], and CLEO-II [67]. The comparison of the pion form factor measured at e^+e^- colliders with the spectral function of the $\tau^- \rightarrow \pi^- \pi^0 \nu_\tau$ decay provides a test of CVC. More theoretical input is necessary to calculate radiative corrections to experimental data and the effects of isospin breaking.

Fig. 27 presents some of the history of the evaluation of the leading contribution $a_\mu(\text{had } 1)$ and the uncertainties involved [69–72].

The ongoing experimental measurements of R mentioned above should reduce the error in $a_\mu(\text{had } 1)$. For our evaluation of $a_\mu(\text{had } 1)$ we take the latest published value [69] which includes both $e^+e^- \rightarrow \text{had}$ data and τ^- decay data and some theoretical assumptions including the validity of perturbative QCD and QCD sum rules.

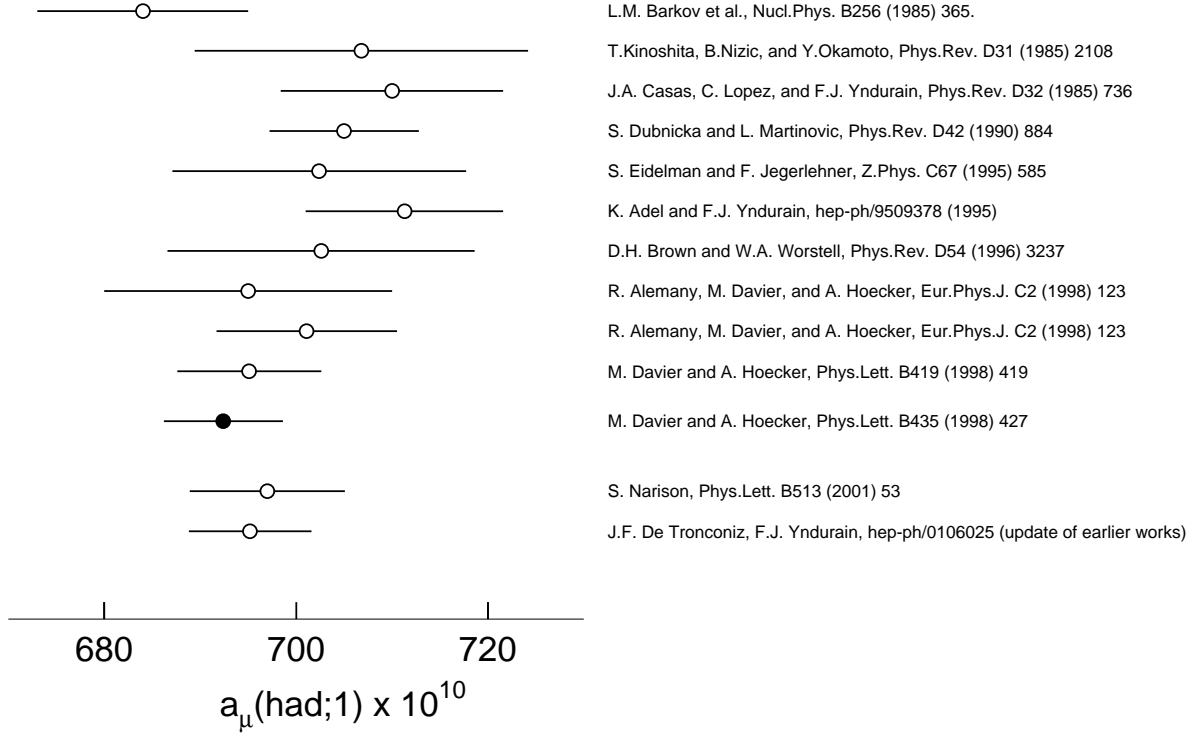


FIG. 27: Evaluations of the leading order hadronic contribution $a_\mu(\text{had } 1)$ ordered by time. The filled circle represents the most recent published value at the time our result from data-taking in 1999 was published. Since then, a new analysis by Narison [71] and an update by Yndurain [72] et al. of earlier works have appeared.

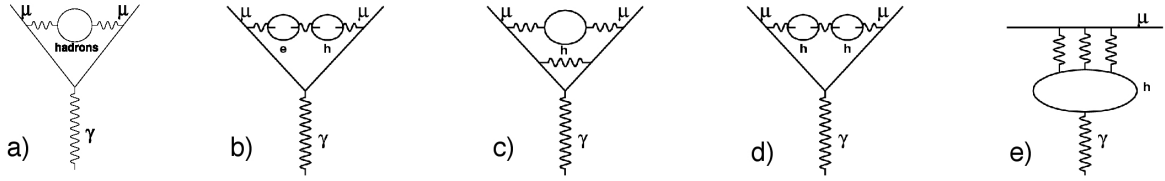


FIG. 28: Feynman diagrams picturing QCD processes contributing to a_μ .

Feynman diagrams for higher order hadronic contributions, $a_\mu(\text{had } 2)$, of relative order α , are shown in Figure 28. Diagrams (b), (c) and (d) can be expressed in terms of the dispersion integral, but the evaluation of diagram (e), which is designated hadronic light-by-light scattering (lbl), has not been successfully expressed in terms of experimentally accessible variables and must be evaluated from QCD. Approximate calculations within the framework of chiral perturbation theory initially [73, 74] gave,

$$a_\mu(\text{had lbl}) = -8.5(2.5) \times 10^{-10} .$$

Subsequent evaluation of the pion-pole contribution using a description of the $\pi^0 - \gamma^* - \gamma^*$ transition form factor based on large- N_c and short-distance properties of QCD gave a value of the same magnitude but opposite sign to the previous calculations [75]. This calculation involved an effective field approach [76], and its result was confirmed [77] in a vector dominance model calculation. Then the authors of the earlier calculations discovered an error in sign [78, 79] so that we take

$$a_\mu(\text{had lbl}) = +8.5(2.5) \times 10^{-10} . \quad (47)$$

The full hadronic contribution is

$$\begin{aligned} a_\mu(\text{had}) &= a_\mu(\text{had 1}) + a_\mu(\text{had 2bcd}) + a_\mu(\text{had lbl}) \\ &= 692.4(6.2) \times 10^{-10} - 10.0(0.6) \times 10^{-10} + 8.5(2.5) \times 10^{-10} \\ &= 690.9(6.7) \times 10^{-10}. \end{aligned} \quad (48)$$

C. Weak Correction

The weak interaction contribution based on the standard electroweak theory is a weak radiative correction to an electromagnetic interaction and arises in lowest order from the single loop diagrams in Figure 29a which involve ν_μ , Z and H particle exchange and where two vertices are weak interaction vertices. The diagrams with the W and Z particles contribute appreciably as given in Eqs. 49 and 50, but since searches establish that the mass of the Higgs particle M_H exceeds 100 GeV, the contribution from the diagram with H is negligible.

$$\begin{aligned} \Delta a_\mu(W) &= \frac{G_\mu m_\mu^2}{8\pi^2 \sqrt{2}} \times \frac{10}{3} \\ &= +38.9 \times 10^{-10}, \end{aligned} \quad (49)$$

$$\begin{aligned} \Delta a_\mu(Z) &= \frac{G_\mu m_\mu^2}{8\pi^2 \sqrt{2}} \times \frac{1}{3} [(3 - 4 \cos^2 \theta_W)^2 - 5] \\ &= -19.4 \times 10^{-10}, \end{aligned} \quad (50)$$

where $G_\mu = 1.16639(1) \times 10^{-5} \text{ GeV}^{-2}$ [80] and $\sin^2 \theta_W = 0.223$.

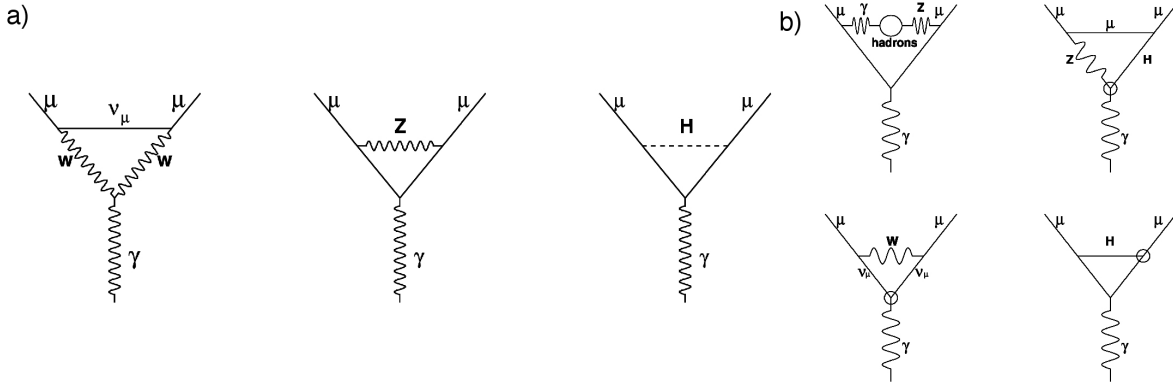


FIG. 29: Feynman diagrams of weak processes contributing to a_μ .

The next order electroweak contribution involving two loop diagrams (Fig. 29b) has been fully calculated. The total weak contribution is

$$\begin{aligned}
 a_\mu(\text{weak}) &= a_\mu^{EW}(\text{1 loop}) + a_\mu^{EW}(\text{2 loop}) \\
 &= 19.5 \times 10^{-10} - 4.4 \times 10^{-10} \\
 &= 15.1(0.4) \times 10^{-10} .
 \end{aligned} \tag{51}$$

Comparison of theory and experiment on $a_\mu(\text{weak})$ will constitute a new and sensitive test of the unified electroweak theory with its prescription for renormalizability. Just as virtual electromagnetic radiative corrections were critical to the development of modern renormalized quantum electrodynamics, so virtual radiative corrections involving both the weak and electromagnetic interactions are most important to the renormalized unified electroweak theory.

Adding the QED, hadronic, and weak contributions we obtain

$$a_\mu(\text{SM}) = 11\,659\,176.6(6.7) \times 10^{-10} \quad (0.6 \text{ ppm}) . \tag{52}$$

IX. COMPARISON OF EXPERIMENT AND THEORY

When the new combined experimental result,

$$a_\mu(\text{expt}) = 11\,659\,203(15) \times 10^{-10} \quad (1.3 \text{ ppm}), \tag{53}$$

was published in the spring of 2001, the most recent, published, and commonly accepted compilation [59] of evaluations from Standard Model theory was

$$a_\mu(\text{SM}) = 11\,659\,159.6(6.7) \times 10^{-10} \quad (0.6 \text{ ppm}). \tag{54}$$

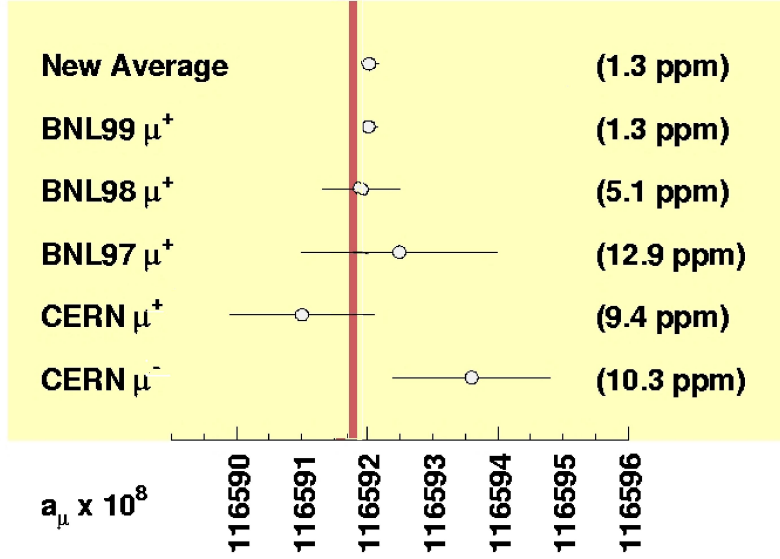


FIG. 30: The value of a_μ from Standard Model theory compared with measurements of a_μ , shown with their total uncertainties.

Subtracting these values gives

$$a_\mu(\text{expt}) - a_\mu(\text{SM}) = 43(16) \times 10^{-10},$$

a difference of about 2.6 times the stated uncertainty.

Since the time of publication, the theoretical value in Eq. 54 has been reexamined and, in particular, the result for the lowest order hadronic contribution $a_\mu(\text{had } 1) = 673.9(6.7) \times 10^{-10}$ [69] has been confirmed [71, 72]. A mistake of sign in the higher order hadronic light-by-light contribution $a_\mu(\text{had lbl}) = -8.5(2.5) \times 10^{-10}$ [73, 74] has recently been revealed [75–77] and recognized [78, 79].

Hence, by simply reversing the erroneous sign, one finds an updated theoretical value,

$$a_\mu(\text{SM}) = 11\,659\,176.6(6.7) \times 10^{-10} \quad (0.6 \text{ ppm}), \quad (55)$$

and for the difference,

$$a_\mu(\text{expt}) - a_\mu^+(\text{SM}) = 26(16) \times 10^{-10}, \quad (56)$$

as visualized in Fig. 30.

X. CONTRIBUTIONS BEYOND THE STANDARD MODEL

Proposed extensions of the standard model will in general contribute to a_μ and hence a comparison of $a_\mu(\text{expt})$ with $a_\mu(\text{SM})$ can in principle detect physics beyond the standard

model [81]. Two classes of extensions can be considered. One postulates compositeness or internal structure for leptons, quarks or gauge bosons and the other involves the introduction of extra groups or particles such as extra gauge bosons, leptoquarks, or supersymmetric particles.

In the standard model leptons, quarks and gauge bosons are assumed to be point-like elementary particles with no internal structure. The magnetic moment of a particle provides a sensitive test for its compositeness, as we have learned for example in the case of the proton. If the muon is composite, the current theoretical viewpoint would imply that

$$\Delta a_\mu \sim \frac{m_\mu^2}{\Lambda^2}, \quad (57)$$

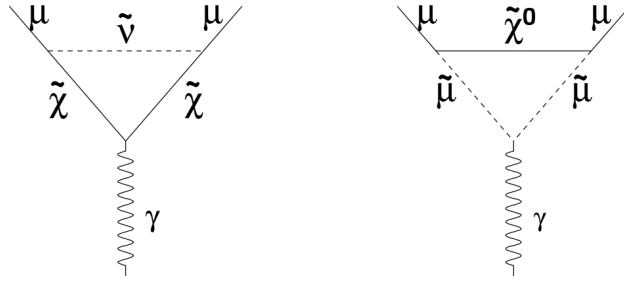
in which Λ is the composite mass scale. Models in which the muon mass is generated by quantum loops also give contributions to a_μ given by Eq. 57 in which Λ then is the scale of new physics responsible for m_μ . Extended technicolor is an example [82, 83]. From the present accuracy in a_μ and the agreement of $a_\mu(\text{expt})$ and $a_\mu(\text{SM})$ we obtain $\Lambda > 1$ TeV. A determination of a_μ to 0.4 ppm, which is the goal of the BNL experiment, would be sensitive to $\Lambda > 4$ to 5 GeV. If the muon were composite, excited muon states would be expected, and from an experimental accuracy for a_μ at 0.4 ppm a sensitivity to m_μ^* up to 400 GeV would be obtained, which is comparable to that from LEP II with $E_{\text{cm}} = 200$ GeV. Compositeness of the W gauge boson or new strong dynamics would lead to an anomalous g_W value $\Delta\kappa$. Determination of a_μ to 0.4 ppm would provide a sensitivity to $\Delta\kappa = 0.04$, which corresponds to $\Lambda_W \sim 2$ TeV, and exceeds considerably the sensitivity possible with LEP II or LHC.

Supersymmetry connects fermions and bosons and introduces supersymmetric partners of known particles (sparticles). The muon g -value is particularly sensitive to supersymmetry [84–86]. Supersymmetry contributes to a_μ through loop diagrams (Fig. 31), which involve smuon-neutralino and sneutrino-chargino loops. In the limit of large $\tan\beta$, which is the ratio of the vacuum expectation values of two Higgs doublets, and for a degenerate spectrum of superparticles with mass \tilde{m} ,

$$a_\mu(\text{SUSY}) \approx 140 \times 10^{-11} \left(\frac{100 \text{ GeV}}{\tilde{m}} \right)^2 \tan\beta. \quad (58)$$

If a difference $a_\mu(\text{exp}) - a_\mu(\text{SM})$ of 3 ppm is found, then for $\tan\beta$ in the range 4 – 40, $\tilde{m} \approx 120 - 400$ GeV. Leptoquarks [87] or theories with extra dimensions [88] could also lead to a difference of $a_\mu(\text{exp}) - a_\mu(\text{SM})$.

A determination of a_μ to 0.4 ppm would provide a sensitivity to m_{susy} for a large value of the ratio of Higgs masses, which is comparable to that from the highest energy collider.

FIG. 31: Feynman diagrams of SUSY processes possibly contributing to a_μ .

Year:	1999	2000	2001	2002
beam:	μ^+	μ^+	μ^-	μ^-
detected events:	2.9×10^9	7×10^9	4×10^9	8×10^9
analyzable events:	1.0×10^9	4×10^9	3×10^9	6×10^9
statistical uncertainty:	0.55 ppm		0.74 ppm	0.5 ppm
systematic uncertainty:	0.5 ppm	0.4 ppm	0.3 ppm	0.3 ppm

TABLE III: Sample sizes and statistical uncertainties from the 1999–2001 data-taking periods, and the projected increase from our proposed 2002 run.

XI. FUTURE

Since its data collection period in 1999, the $g - 2$ collaboration has taken data on μ^+ in 2000 and — its first — data on μ^- in 2001. The analyses of these data are underway, and we presently foresee their completion with sample sizes of $4 \cdot 10^9$ positrons (2000) and $3 \cdot 10^9$ electrons (2001), corresponding to statistical uncertainties of 0.62 ppm and 0.74 ppm, respectively (cf. Table III). If the results for a_μ^+ and a_μ^- are found to be in agreement, as is expected from CPT invariance, the values will be combined. The combined statistical uncertainty from data collection in 1999–2001 is then projected to reach 0.44 ppm.

To reduce the systematic uncertainties from the 0.5 ppm level achieved in the 1999 running period,

- we replaced the inflector magnet before starting the data collection in 2000, thus further improving the field homogeneity and measurement,
- we improved on the trolley field measurements by additional calibrations against a plunging probe during the running periods, and by improved position measurement,
- we added a sweeper magnet to the beamline to reduce AGS background in the course

of the 2000 running period,

- we reduced the uncertainty due to pileup,
- we reduced muon losses during the $g - 2$ measurement time, and
- we improved our understanding of the effects of coherent beam motion, and adjusted the operational settings of our ring accordingly.

As the result of these efforts combined, we tentatively foresee a reduction of the systematic uncertainties by as much as 40% to about 0.3 ppm on our future results.

A proposal for extended running for four months in the fall of 2002 and winter of 2003 to complete the muon $g - 2$ experiment by:

- balancing the statistical uncertainties for the samples on μ^+ and μ^- , and
- balancing the statistical uncertainty of the combined result with the systematic uncertainties at the design level of about 0.3 ppm,

has been successfully defended to the Brookhaven Program Advisory Committee and is presently pending its funding.

The evaluation of a_μ from Standard Model theory has achieved an accuracy of about 0.6 ppm, which results predominantly from uncertainties in the lowest order hadronic contribution. This contribution is evaluated from a dispersion relation and from cross section measurements, and is bound to improve with the inclusion of more and more precise data, particularly on the ratio $R(s) = \sigma_{\text{total}}(e^+e^- \rightarrow \text{hadrons})/\sigma_{\text{total}}(e^+e^- \rightarrow \mu^+\mu^-)$ from Novosibirsk and Beijing. The treatment of τ -decay data to evaluate $a_\mu(\text{had } 1)$ will benefit from further study of CVC.

The experimental value and theoretical prediction for a_μ continue to have their role at the frontiers in particle physics, provided both are pursued to best achievable accuracy and regardless the difference of their values.

XII. EARLY HISTORY OF THE EXPERIMENT AT BNL; OUR COLLABORATION

After the second CERN experiment was done, I (VWH) had considered the possibility of measuring muon $g - 2$ using a superconducting storage ring, but then the third famous CERN experiment with the magic γ got under way.

It was during a workshop at Los Alamos in 1982 on LAMPF II, which was to be a proton accelerator of 40 GeV with very high intensity, that I again considered measuring $(g_\mu - 2)$.

The third CERN experiment had been done, achieving an accuracy of 10 ppm for μ^+ and μ^- individually, and hence, a combined precision of 7 ppm for the muon. This 7 ppm uncertainty was attributed predominantly to the statistical error. The quoted theoretical error at the time was 8 ppm; it arose principally from uncertainty in the hadronic contribution to $g_\mu - 2$. In the context of the LAMPF II workshop, where a proton beam intensity 100 times that used in the CERN experiment was a design parameter, it seemed reasonable that the statistical error could be greatly reduced.

Walter Lysenko of Los Alamos National Laboratory and I wrote a contribution to the LAMPF II Workshop on the possibility of a new muon $g - 2$ experiment. However, a high-intensity proton beam was then available from the AGS at BNL, and BNL had plans to increase the intensity still further. The AGS seemed a more real possibility.

After the completion of the CERN experiment, an interesting article had been published by R.W. Williams, one of the participants in the experiment. It was entitled "Muon $g - 2$ – the Last Word." Williams made two very reasonable points to support his conclusion. First, an improved experiment would be very difficult and expensive; second, the uncertainty in the theoretical value was at the same level as the experimental uncertainty and would be hard to improve.

Because of the importance of having a precise value for $(g_\mu - 2)$, despite William's observations, I considered two approaches for an improved experiment:

- The use of an intense polarized μ^+ beam of 30 MeV/c available at LAMPF in a bottle-type experiment similar to the free-electron $g_e - 2$ experiment by Rich at Michigan,
- An experiment similar to the CERN III experiment, using either an iron or a superconducting magnet.

During 1983, Gordon Danby of BNL and I considered the design of a CERN III-type experiment based on a superconducting magnet, and I gave a seminar at Columbia while I was on leave from Yale. In summer 1984, a workshop was organized at BNL where we had a large and interesting group (Fig. 32), including the principal members of the CERN III experiment.

A letter of intent was submitted to BNL in 1984, and by 1985 our proposal, based now on a superferic magnet, had received first-stage approval. A substantial collaboration was developing, which included KEK in Japan and the Budker Institute for Nuclear Physics in Novosibirsk. But funds for the necessary research and development were minimal. Indeed, the first money to support BNL engineers for design of the superferic storage ring came from KEK in the context of the US-Japan Collaboration in High Energy Physics. Hiromi



FIG. 32: At Brookhaven National Laboratory, summer 1984. *Standing, from left:* Gordon Danby, John Field, Francis Farley, Emilio Picasso, and Frank Krienen; *kneeling from left:* John Bailey, Vernon Hughes, and Fred Combley.

Hirabayashi of KEK was the leader of the Japanese group. Akira Yamamoto provided invaluable help in the design of the large superconducting coils. Eventually the Japanese group supplied all the superconducting cable and the high-quality iron pole pieces. Yamamoto also provided the superconducting inflector.

We shared with Novosibirsk an interest in the hadronic contribution to the muon $g - 2$ value. Close relations were established with Lev Barkov, a leader in the Budker Institute for Nuclear Physics (BINP), and with his VEPP 2M detector group. Their measurements of the hadron production cross section $\sigma(e^+e^- \rightarrow \text{hadrons})$ with the VEPP 2M collider have played the lead role in providing improved knowledge of the hadronic contribution to the anomalous moment. It is now known to about 0.7 ppm, a factor of 10 better than in 1984. Some physicists from BINP became collaborators on our muon $g_\mu - 2$ experiment at BNL.

BNL did an outstanding job in the design and construction of the muon storage ring under the leadership of Jim Cullen. Still, in the beginning, BNL Physics Department members were not in our collaboration and my colleague and good friend Bob Adair, who was then Associate Director for High Energy Physics at BNL, would tell me that $(g_\mu - 2)$ was not a BNL experiment. The full development of the muon $g - 2$ experiment at BNL came rather

slowly, both because of the difficulty of this precision experiment and because of lack of funds. Eventually a strong group — presently about 70 physicists from institutes in Germany (Heidelberg University), Japan (KEK, Tokyo Institute of Technology), Russia (BINP), and the United States (Boston University, Brookhaven National Laboratory, Cornell University, Fairfield University, University of Illinois, University of Minnesota, and Yale University) — developed, with Lee Roberts as co-spokesman, Bill Morse as resident spokesman, and Gerry Bunce as project manager.

XIII. ACKNOWLEDGEMENTS

This research was supported in part by the U.S. Department of Energy, the U.S. National Science Foundation, the German Bundesminister für Bildung und Forschung, the Russian Ministry of Science, and the US-Japan Collaboration in High Energy Physics.

-
- [1] W. Gerlach and O. Stern, *Zeits. f. Physik* **8**, 110 (1924).
 - [2] S. Goudsmit and G.E. Uhlenbeck, *Naturwissenschaften* **13**, 953 (1925); S. Goudsmit and G.E. Uhlenbeck, *Nature* **117**, 264 (1926).
 - [3] R. Frisch and O. Stern, *Zeits. f. Physik* **85**, 4 (1933); I. Estermann and O. Stern, *ibid* **85**, 17 (1933).
 - [4] N.F. Ramsey, *Molecular Beams*, Clarendon Press, Oxford, 1956.
 - [5] P. Kusch and H.M. Foley, *Phys. Rev.* **72**, 1256 (1947).
 - [6] W.E. Lamb, Jr. and R.C. Retherford, *Phys. Rev.* **72**, 241 (1947).
 - [7] J.E. Nafe, E.B. Nelson, and I.I. Rabi, *Phys. Rev.* **71**, 914 (1947).
 - [8] J. Schwinger, *Phys. Rev.* **73**, 416 (1948).
 - [9] G. Charpak, F.J.M. Farley, R.L. Garwin, T. Muller, J.C. Sens, and A. Zichichi, *Phys. Lett.* **1**, 16 (1962).
 - [10] V.W. Hughes and T. Kinoshita, *Rev. Mod. Phys.* **71** Centenary 1999 S 1333.
 - [11] R.S. Van Dyck, Jr., P.J. Schwinberg, and H.G. Dehmelt, *Phys. Rev. Lett.* **59**, 26 (1987); R.S. Van Dyck, Jr., P.J. Schwinberg, and H.G. Dehmelt, *Phys. Rev.* **D34**, 722 (1986); R.S. Van Dyck, Jr., P.J. Schwinberg, and H.G. Dehmelt, *Phys. Rev. Lett.* **38**, 310 (1977); R.S. Van Dyck, Jr. in *Quantum Electrodynamics*, ed. T. Kinoshita (World Scientific, Singapore, 1990) p. 322.
 - [12] T. Kinoshita in *Quantum Electrodynamics*, ed. T. Kinoshita (World Scientific, Singapore, 1990) p. 218.
 - [13] J. Bailey et al., *Nuovo Cimento* **A9**, 369 (1972).
 - [14] J. Bailey et al., *Nucl. Phys.* **B150**, 1 (1979).
 - [15] F. Combley and E. Picasso, *Phys. Rept.* **14**, 1 (1974).
 - [16] F.J.M. Farley and E. Picasso, *Ann. Rev. Nucl. Part. Sci.* **29**, 243 (1979).

- [17] G. Gabrielse, J. Tan, and L.S. Brown in Quantum Electrodynamics, ed. T. Kinoshita (World Scientific, Singapore, 1990) p. 389.
- [18] T. Kinoshita in The Gregory Breit Centennial Symposium, eds. V.W. Hughes, F. Iachello, and D. Kusnezov (World Scientific, Singapore, 2001) p. 15.
- [19] S. Lapporta and E. Remiddi, Phys. Lett. **B379**, 283 (1996).
- [20] P.J. Mohr and B.N. Taylor, Rev. Mod. Phys. **72**, 351 (2000).
- [21] T. Kinoshita, Rept. Prog. Phys. **59**, 1459 (1996).
- [22] M.C. George, L.D. Lombardi, and E.A. Hessels, Phys. Rev. Lett. **87**, 173002 (2001).
- [23] T.M. Hensley, A. Wicht, B.C. Young, and S. Chu in Atomic Physics 17 eds. E. Arimondo, P. De Natale, and M. Inguscio. (AIP, New York, 2001) p. 43.
- [24] The $g - 2$ collaboration: R.M. Carey et al., Phys. Rev. Lett. **82**, 1132 (1999).
- [25] W. Liu et al., Phys. Rev. Lett. **82**, 711 (1999).
- [26] T. Kinoshita, hep-ph/9808351; T. Kinoshita and M. Nio in Frontier Tests of Quantum Electrodynamics and Physics of the Vacuum, eds. E. Zavattini, D. Bakalov, and C. Rizzo (Heron Press, Sofia, 1998) p. 151, and references therein.
- [27] G.K. Green and E.D. Courant in Encyclopedia of Physics, ed. S. Flugge (Springer Verlag, Heidelberg, 1959)
- [28] S.Y. Lee, Accelerator Physics, (World Scientific, Singapore, 1999).
- [29] L.H. Thomas, Phil. Mag. **3**, 1 (1927).
- [30] V. Bargmann, L. Michel, and V.A. Telegdi, Phys. Rev. Lett. **2**, 435 (1959).
- [31] J.D. Jackson, Classical Electrodynamics (John Wiley and Sons, New York, 1962).
- [32] B.W. Montague, Physics Reports **113**, (1984).
- [33] J.S. Bell, CERN-75-11, 38p (1975).
- [34] F.J.M. Farley and E. Picasso, in Quantum Electrodynamics, ed. T. Kinoshita (World Scientific, Singapore, 1990) p. 479.
- [35] W. Lysenko, Ph.D. Thesis, Yale University (1972).
- [36] D.A. Edwards and M.J. Syphers, An Introduction to the Physics of High Energy Accelerators, (John Wiley and Sons, New York, 1992).
- [37] F. Krienen, D. Loomba, and W. Meng Nucl. Instrum. Meth. **A283**, 5 (1989).
- [38] G.T. Danby et al., Nucl. Instrum. Meth. **A457**, 151 (2001).
- [39] R. Prigl et al., Nucl. Instrum. Methods **A374**, 118 (1996).
- [40] A. Grossmann, Ph.D. Thesis, Universität Heidelberg (1998).
- [41] S.J. Redin et al., Nucl. Instrum. Meth. **A473**, 260 (2001).
- [42] X. Fei, V.W. Hughes, and R. Prigl, Nucl. Instrum. Meth. **A394**, 349 (1997).
- [43] W.D. Phillips et al., Metrologia **13**, 179 (1979).
- [44] P.F. Winkler, D. Kleppner, T. Myint, and F.G. Walther, Phys. Rev. **A5**, 83 (1972).
- [45] W.E. Lamb Jr., Phys. Rev. **60**, 817 (1941).
- [46] H. Grotch and R.A. Hegstrom, Phys. Rev. **A4**, 59 (1971).
- [47] B.W. Petley et al., Metrologia **20**, 81 (1984).
- [48] S.A. Sedykh et al., Nucl. Instrum. Meth. **A455**, 346 (2000).
- [49] S. Dhawan, V.W. Hughes, D. Kawall, W. Liu, and J. Pretz, Nucl. Instrum. Meth. **450**, 391 (2000).

- [50] LORAN-C User's Handbook, 1992, Superintendent of Documents, U.S. Government Printing Office #050-012-00331-9.
- [51] W.H. Press, S.A. Teukolsky, W.T. Vetterling, and B.P. Flannery, Numerical Recipes in C: The Art of Scientific Computing (Cambridge University Press, 1993), p. 645.
- [52] The $g - 2$ collaboration: H.N. Brown et al., Phys. Rev. **D62**, 091101 (2000).
- [53] H.E. Ahn, Ph.D. Thesis, Yale University (1992).
- [54] S.I. Redin, Ph.D. Thesis, Yale University (1999).
- [55] J. Kindem, Ph.D. Thesis, University of Minnesota (1998).
- [56] A. Trofimov, Ph.D. Thesis, Boston University (2001).
- [57] L.H. Duong, Ph.D. Thesis, University of Minnesota (2001).
- [58] The $g - 2$ collaboration: H.N. Brown et al., Phys. Rev. Lett. **86**, 2227 (2001).
- [59] A. Czarnecki and W.J. Marciano, Nucl. Phys. (Proc. Suppl.) **B76**, 245 (1999).
- [60] T. Kinoshita and W.J. Marciano in Quantum Electrodynamics, (World Scientific, Singapore, 1990) p. 419.
- [61] T. Kinoshita, private communication (2001).
- [62] L.M. Barkov et al., Nucl. Phys. **B256**, 365 (1985).
- [63] The CMD-2 collaboration: R.R. Akhmetshin et al., Phys. Lett. **B475**, 190 (2000); *ibid* **B527**, 161 (2002).
- [64] Z.G. Zhao, Int. J. Mod. Phys. **A15**, 3739 (2000) and The BES collaboration: J.Z. Bai, et al., Phys. Rev. Lett. **84**, 594 (2000).
- [65] The Aleph collaboration: R. Barate et al., Z. Phys. **C76**, 15 (1997); Eur. Phys. J. **C4**, 409 (1998).
- [66] The Opal collaboration: K. Ackerstaff et al., Eur. Phys. J. **C7**, 571 (1999).
- [67] The CLEO collaboration: S. Anderson et al., Phys. Rev. **D61**, 112002 (2000).
- [68] S.I. Eidelman, Nucl. Phys. (Proc. Suppl.) **B98**, 281 (2001).
- [69] M. Davier and A. Höcker, Phys. Lett. **B435**, 427 (1998).
- [70] K. Melnikov, Int. J. Mod. Phys. **A16**, 4591 (2001).
- [71] S. Narison, Phys. Lett. **B513**, 53 (2001), *erratum-ibid.* **B526** 414, 2002.
- [72] J.F. De Troconiz and F.J. Yndurain, FTUAM-01-08 (2001), hep-ph/0106025v5.
- [73] J. Bijnens, E. Pallante, and J. Prades, Nucl. Phys. **B474**, 379 (1996).
- [74] M. Hayakawa and T. Kinoshita, Phys. Rev. **D57**, 465 (1998).
- [75] M. Knecht and A. Nyffeler, CPT-2001-P-4253 (2001), hep-ph/0111058.
- [76] M. Knecht, A. Nyffeler, M. Perrottet, and E. De Rafael, Phys. Rev. Lett. **88**, 071802 (2002).
- [77] I. Blokland, A. Czarnecki, and K. Melnikov, Phys. Rev. Lett. **88**, 071803 (2002).
- [78] M. Hayakawa and T. Kinoshita, KEK-TH-793 (2001), hep-ph/0112102.
- [79] J. Bijnens, E. Pallante, and J. Prades, LU-TP-01-37 (2001), hep-ph/0112255.
- [80] The Particle Data Group: D.E. Groom et al., The European Physical Journal **C15**, 1 (2000).
- [81] A. Czarnecki and W.J. Marciano, Phys. Rev. **D64** 013014 (2001).
- [82] W.J. Marciano, in Particle Theory and Phenomenology, eds. K. Lassila et al., (World Scientific, Singapore, 1996) p. 22.
- [83] P. Mery, S.E. Moubarik, M. Perrottet, and F.M. Renard, Z. Phys. **C46**, 229 (1990).
- [84] T. Moroi, Phys. Rev. **D53**, 6565 (1996); S. Komine, T. Moroi, M. Yamaguchi, Phys. Lett.

- B506**, 93 (2001).
- [85] U. Chattopadhyay and P. Nath, Phys. Rev. **D53**, 1648 (1996); U. Chattopadhyay and P. Nath, Phys. Rev. Lett. **86**, 5854 (2001).
 - [86] J.L. Lopez, D.V. Nanopoulos and X. Wang, Phys. Rev **D49**, 366 (1994); J.R. Ellis, D.V. Nanopoulos, K.A. Olive, Phys. Lett. **B508**, 65 (2001).
 - [87] S. Davidson, D. Bailey, and B.A. Campbell, Zeits. f. Physik **C61**, 613 (1994); G. Couture and H. König, Phys. Rev. **D53**, 555 (1996); D. Chakraverty, D. Choudhury, and A. Datta, Phys. Lett. **B506**, 103 (2001); K. Cheung, Phys. Ref. **D64**, 033001 (2001).
 - [88] T. Appelquist and B.A. Dobrescu, Phys. Lett. **B516**, 85 (2001).